Brain resident macrophages regulate sleep, with repopulated ones being unable to reestablish the original sleep circuits

Ali Seifinejad[1*], Gianni Monaco[1], Mojtaba Bandarabadi[2], Meriem Haddar[2], Saskia Wundt[1], Victoria Wingert[3], Luciana Hannibal[3], Thomas Blank[1], Mehdi Tafti[2], and Marco Prinz[1, 4*,]

[1] Institute of Neuropathology, Faculty of Medicine, University of Freiburg, Freiburg, Germany

[2] Department of Biomedical Sciences, University of Lausanne, Lausanne, Switzerland

[3] Department of General Paediatrics, Adolescent Medicine and Neonatology, Laboratory of Clinical Biochemistry and Metabolism, Medical Center, University of Freiburg, Faculty of Medicine, Freiburg, Germany

[4] Signalling Research Centres BIOSS and CIBSS, University of Freiburg, Freiburg, Germany

[*]Correspondence to:

Marco Prinz: marco.prinz@uniklinik-freiburg.de or

Ali Seifinejad: ali.seifinejad@mail.ch

Summary

Brain resident macrophages such as microglia and CNS-associated macrophages (CAMs) are already established before birth and play therefore a crucial role for normal brain functioning during development. However, their involvement in fine-tuning complex physiological functions such as vigilance states (VS) after birth remains poorly understood. Here, we investigated the reciprocal interaction of microglia and VS using multimodal high throughput transcriptional, electrophysiological and metabolomic profiling in mice. We found that sleep deprivation caused severe transcriptional changes in microglia and CAMs and absence of the wake-promoting neuropeptides hypocretin/orexin intensified these effects. Depletion of embryonic microglia robustly increased sleep quantity during the active period, while decreased sleep quality that was reflected in reduced power of brain sleep oscillations. Unexpectedly, subsequent repopulation by postnatal microglia failed to reestablish normal sleep-wake patterns, and even induced additional abnormalities such as sleep fragmentation. Moreover, we found a substantial excitatory-inhibitory synaptic imbalance following microglia depletion, which was not normalized after microglial repopulation and even lead to an increase of inhibitory synapses in the brain. At the metabolite level, we observed a distinct metabolite pattern after microglia depletion, which largely returned to normal levels after repopulation. Our findings suggest a so far largely unknown interaction between microglia and brain VS and emphasizes striking functional differences between embryonic and postnatal-derived microglia, thereby potentially paving the way for the further exploration of microglia of different origin and their roles in sleep disorders and synaptic connectivity.

Keywords: Microglia; CAM, vigilance states, sleep; HCRT

50 **Introduction**

51 Tissue-resident myeloid cells in the CNS comprising parenchymal microglia and CAMs [1-4], play
52 significant roles in pathology and protecting the CNS from damage [5]. Although the function of
53 CAMs in regulating brain function is not well understood, microglia participate in a range of
54 physiological functions including synaptic pruning [6], remodeling and displacement [7], pain control
55 [8,9], learning and memory [10,11], neurogenesis [11], and sleep-wake regulation [12].

56 Microglial cells and leptomeningeal macrophages (as part of the CAMs) are derived from prenatal
57 sources known as erythormyeloid precursors that engraft into the developing CNS [13,14] and
58 facilitate the establishment of neuronal networks especially until the first postnatal weeks [6]. If
59 embryonic microglial cells are depleted during adulthood, they repopulate from surviving
60 endogenous cells [15]. The *de novo* establishment of the micoglial networks occurs by surviving
61 cells through clonal expansion [16] and these postnatal-derived microglial cells exhibit a different
62 transcriptinal signature [17]. However, whether these adultood-derived microglia exhibit any
63 functional differences to orginal embryo-derived ones is currently largely unknown.

64 VS are divided into wakefulness, non-rapid eye movement sleep (NREMS), and rapid eye
65 movement sleep (REMS), which are dynamic complex states and vital for the normal brain
66 functioning. They are measured using electroencephalogram (EEG) and characterized by
67 different brain oscillations, e.g. delta waves (0.5-4Hz) for NREMS and theta waves (6-9Hz) for
68 REMS in rodents. Dysregulation of VS is associated with a variety of diseases such as sleep
69 disorders, cardiovascular and neurodegenerative disorders such as Alzheimer's disease (AD)
70 [18,19]. VS regulation and sleep oscillatory patterns rely on a complex CNS connectivity, and different
71 cell types, mainly neuronal populations interact with each other (via synaptic connections and
72 neurotransmitter release) to fine-tune the regulation of VS and brain oscillations. Among the major
73 neuropeptides and neurotransmitters involved in VS regulation are hypocretin/orexin (HCRT) and
74 melanin-concentrating hormone neurons (MCH) in the lateral hypothalamus (LH), serotonin (5HT)

and noradrenaline (NA) in the brainstem (BS), and acetylcholine in the BS and basal forebrain (BF), and midbrain dopaminergic neurons [20,21].

While a few studies have demonstrated a bidirectional relationship between embryo-derived microglia and the VS [12,22-24], a comprehensive understanding of how these two compartments modulate each other is still lacking. Specifically, we do not yet know the transcriptional signature of microglia and CAMs in response to sleep loss, both in healthy individuals and in disease conditions, such as narcolepsy with cataplexy, where patients have undetectable HCRT neuropeptide levels. This deficiency in HCRT neuropeptide is largely thought to be immune-mediated, and there have been reports of increased MHC-II molecule expression in microglia at the onset of canine narcolepsy [25]. Additionally, it remains unclear whether adulthood-derived microglia are capable of re-establishing neural circuitries in the same manner as prenatal microglial cells, including synaptic plasticity and neurochemical balance, which are crucial for the normal VS regulation.

Here, we first studied the impact of sleep deprivation on the transcriptional signature of microglia and CAMs in both wild-type (WT) and HCRT cell-ablated narcolepsy mouse model (*Hcrt-ataxin-3*) mice. Next, through in-depth analysis, we explored whether the absence of embryo-derived microglia and CAMs influences normal VS patterns and whether repopulated postnatal microglia and CAMs can normalize these patterns. Finally, we investigated how the absence of microglia and CAMs affects brain network connectivity and neurochemistry.

Results

HCRT neuron ablation significantly alters transcriptional profile of microglia and CAMs in response to sleep loss

Sleep deprivation (SD) induces functional alterations in microglia [26,27], however its impact on the transcriptional profile of microglia and CAMs has not yet been documented. Furthermore, it is uncertain whether any of the substances that regulate VS mentioned earlier could worsen or alleviate the impacts of sleep deficiency on microglia and CAMs. To better understand this, we isolated microglia and CAMs from the cortex and hypothalamus, which are the two main sleep-regulating centers, of both wild-type (WT) and *Hcrt-ataxin-3* mice (hereafter referred to as Ataxin mice) [28]. HCRT neurons play a central role in regulating wakefulness [29] and waking behaviors that drive sleep need [30], and HCRT deficiency is a hallmark biomarker of human narcolepsy with cataplexy. By studying these mice, we aimed at determining whether the lack of HCRT neuropeptide has any influence on the transcriptional profile of microglia and CAMs in response to SD possibly contributing to narcolepsy with cataplexy phenotype.

We deprived mice of sleep for 6 h (starting from light onset) and immediately afterward, isolated microglia ($CD11b^+$, CD45intermediate) and CAMs ($CD11b^+$, $CD206^+$) from the cortex and hypothalamus of both WT and Ataxin mice (Figure 1A, B). The control group was not sleep deprived. We extracted RNA and performed bulk RNA sequencing (RNA-seq) to compare their transcriptome across different conditions. After 6 hours SD, no changes were observed in expression of microglial core genes (*Hexb*, *P2ry12*, *Trem2*, and *TMEM119*) across the cortex and hypothalamus (Supplementary Fig. 1A). Furthermore, we did not observe any transcriptional changes when comparing microglia from wild-type (WT) and Ataxin mice under normal conditions, and only two *Lyz2* and *Slc31a2* genes were differentially regulated after SD in these two mouse lines (Supplementary Fig. 1B). When comparing the microglial transcriptome between SD and control conditions across the cortex and hypothalamus of WT mice, we observed many differentially expressed genes (DEGs) (110 genes) (Figure 1C, E). However, the same

120 comparison in Ataxin mice resulted in a larger number of DEGs compared to WT mice (270 genes)
121 (Figure 1D, F). This finding is intriguing because it suggests that the HCRT neuropeptide directly
122 or indirectly interacts with and modulates microglia during enforced wakefulness (SD). While we
123 did not detect the expression of HCRT receptors in microglia, we observed the expression of
124 downstream circuit receptors, including noradrenaline and serotonin receptors, in microglia. One
125 such gene is the beta-2 adrenergic receptor (*Adrb2*), which is predominantly expressed in
126 hypothalamic microglia compared to cortical microglia (Supplementary Fig. 1C). We also
127 observed that SD primarily affects cortical, rather than hypothalamic microglia in Ataxin mice. In
128 WT mice, however, the hypothalamic microglia are more impacted by SD (Supplementary Fig. 2),
129 indicating that the cortical microglia are more susceptible to the lack of HCRT.
130 Several genes were primarily regulated under the SD condition, such as *Cirbp*, *Ighd*, and *Npnt*
131 (Fig. 1G). Additionally, we found genes that were mainly expressed in the hypothalamus
132 compared to the cortex (Fig. 1H). Furthermore, we observed that genes such as *Sgk1* and *Pecr*
133 were largely regulated after SD in the hypothalamus but not in the cortex, suggesting structure-
134 specific microglia changes after SD (Fig. 1I). Lastly, we found genes that were exclusively
135 regulated in Ataxin mice like *Slc31a2*, *Lyz2*, and *Ccl4* (Fig. 1J). Gene set enrichment analysis of
136 the DEGs in WT mice revealed an enrichment of pathways related to protein folding, such as
137 "Positive regulation of protein folding" (Supplementary Fig. 3A). In contrast, the analysis of DEGs
138 in Ataxin mice indicated an enrichment of pathways like "Virion attachment to host cell"
139 (Supplementary Fig. 3B). This finding is intriguing, as the 2009 H1N1 vaccination has been linked
140 to a high incidence of narcolepsy disease [31], and it remains to be carefully investigated whether
141 microglia play a role in this process.
142 We next investigated how SD affects the transcriptome of CAMs in WT and Ataxin mice. As CAMs
143 are not abundant in the brain, we sorted them from the entire brain. Our results revealed that 6
144 hours of SD induced numerous DEGs in CAMs sorted from WT mice compared to the control
145 condition (Fig. 1K). Among these DEGs were the *App* and *Lyve1* genes (Fig. 1L), both of which

146 have been linked to Alzheimer's disease (AD) pathogenesis [32,33]. It is intriguing to note that *Lyve1*
147 gene expression almost tripled after 6 hours of SD. Gene set enrichment analysis of DEGs of
148 CAMs in WT mice revealed enrichment for pathways related to AD, including positive regulation
149 of tau-protein kinase activity (Supplementary Fig. 3C). Nevertheless, we were astonished to
150 discover an opposing result of only a small number of DEGs while contrasting SD versus control
151 in CAMs of Ataxin mice (Fig. 1M), as we witnessed numerous DEGs in microglia of Ataxin mice
152 after SD. As the DEGs found in CAMs of WT mice have been implicated in AD, a thorough
153 literature search uncovered a study by Roh et al. [34] indicating that a null mutation in the *Hcrt* gene
154 in an AD mouse model leads to a significant reduction in Aβ pathology in the brain. It can be
155 speculated that this effect is mediated by CAMs and not microglia.
156 Overall, these data indicate that both microglia and CAMs transcriptional networks are modulated
157 by VS and HCRT neuropeptide that regulates VS, suggesting a reciprocal interaction between
158 both systems.
159
160 **Repopulated adulthood-derived microglia fall short in rebuilding normal NREMS circuitry**
161 We demonstrated that there is an interaction between brain-resident macrophages and VS, which
162 leads us to expect that brain-resident macrophages are also involved in regulating sleep. While
163 there is a limited number of studies examining the regulatory role of microglia in VS [12,23,35], a
164 comprehensive understanding of this regulation, as well as the specific parameters of the VS
165 affected by brain-resident macrophages, remains unclear. To address this, we depleted microglia
166 from the brains of mice for two weeks using colony-stimulating factor 1 receptor (CSF1R) inhibition
167 via PLX5622 [36] and allowed them to repopulate for four weeks (Fig. 2A). CSF1 receptor is vital
168 for microglia survival. Antagonizing it severely depletes microglia within three days, and upon the
169 termination of treatment, a fast repopulation can be observed within a few days [17]. We observed
170 substantial microglia depletion (>86%) after two weeks of PLX5622 treatment and complete
171 repopulation four weeks after withdrawal (Fig. 2B, C).

172 We recorded EEG signals before depletion (control), after depletion and after repopulation (Fig.
173 2A). We included the repopulation phase to determine if it restores any potential changes in the
174 VS induced after microglia depletion. Since CSF1 inhibition also depletes CAMs [37], the effects we
175 report here are due to the depletion of both cell types, which we refer to collectively as MG. Our
176 experimental conditions therefore included control, MG-Dep (microglia/CAM depleted), and MG-
177 Repop (microglia/CAM repopulation). To evaluate the distribution of vigilance states, we
178 employed our standard sleep/wake phenotyping protocol [38], with two days of baseline (which were
179 averaged and presented as one day in the figures) and in the third day we had 6 hours of SD
180 (ZT0-ZT6) and 18 hours of recovery (Fig. 1D). In baseline conditions, all experimental mice
181 demonstrated the characteristic rhythmic diurnal behavior, with higher levels of wakefulness
182 during the dark period and higher levels of NREMS during the light period and exhibited the
183 increase in NREMS amounts in response to SD (Fig. 1E, F). The distribution of wakefulness and
184 NREMS in all experimental groups was typical, and the appearance of one state occurred at the
185 cost of the other. However, significant differences (NREMS increase) were observed in the
186 baseline dark period when comparing the MG-Dep to the control condition. Interestingly, the
187 repopulation of MG did not normalize this effect (Control: 12.75±0.72 min, MG-Dep: 16.78±0.77
188 min, MG-Repop: 16.54±0.70 min, mean ± SEM) (Fig. 2E, F, bottom panels). Additionally, during
189 the dark period, there was a notable reduction in wakefulness (Fig. 2E, F, top panels).
190 To gain insight into the homeostatic regulation of sleep in different mice groups and to determine
191 whether increased sleep is due to an increased need for sleep, we analyzed the time course of
192 NREMS EEG delta power (1-4 Hz, mainly referred to as sleep need) across our 3-day recordings.
193 All mice groups showed a typical decline in delta power during the light period and a strong
194 rebound after SD, indicating the homeostatic regulation of sleep need in all groups (Fig. 2G).
195 However, the buildup in delta power during the baseline dark period was significantly lower in
196 MG-Dep and MG-Repop mice compared to WT mice (Fig. 2G). This attenuation was more
197 pronounced in MG-Repop mice and may be partly related to increased sleep during the baseline

198 dark period (Fig. 2E, lower panel). However, when mice were exposed to enforced wakefulness
199 (SD), the EEG delta power significantly increased and this effect was more noticeable in the MG-
200 Repop condition (Fig. 2G). Altogether, these data indicate a deficient buildup in homeostatic sleep
201 need during the waking period.
202 Spectral analysis of NREMS showed that MG-Dep mice exhibited higher slow-delta (1-2 Hz)
203 activity compared to control mice during the baseline light period (Fig. 2H, left). This frequency
204 band appears to be more affected, even in MG-Repop mice, as it was significantly increased
205 during the recovery light period after the mice were exposed to SD (Fig. 2I, left). The brain circuits
206 that are more vulnerable to microglia depletion and repopulation, resulting in those changes in
207 EEG power, are still unknown. However, our previous study has shown an increase in slow delta
208 activity during the light period in 5HT transporter knockout (5HTT KO), 5HTT; Hcrt double KO,
209 and DR_Hcrt1&2cKO mice [38]. In contrast, the fast delta (3-4 Hz) was blunted during both baseline
210 and recovery light periods and only in the MG-Dep condition (Fig. 2H, I, left). During the baseline
211 dark period, large blunting was observed in both MG-Repop (1.5-3.5Hz) and MG-Dep (3-5.5Hz)
212 conditions. These deficits remained nearly the same during the recovery dark period, indicating
213 that NREMS of both experimental mice appears to be largely shallower (Fig. 2H, I, right).
214 Collectively, it can be concluded that the presence of MG is necessary for the precise regulation
215 of fast and slow-delta power as a proxy for the sleep homeostatic process. MG repopulation not
216 only fails to restore NREMS regulation but worsens it.
217 To further determine whether the increase in NREMS is due to consolidation of this state or more
218 NREMS episodes, we conducted the sleep fragmentation analysis. We found that while MG-Dep
219 mice have similar sleep bout duration patterns as the control condition, MG-Repop mice showed
220 a large number of shorter NREMS bouts (16 seconds [Control: 6.7±0.63, MG-Dep: 6.8±0.7, MG-
221 Repop: 9.84±1.12]) and 64 seconds [Control: 12.12±1.15, MG-Dep: 11.02±0.81, MG-Repop:
222 17.63±1.2]) and fewer longer NREMS bouts (>256 seconds [Control: 1.96±0.28, MG-Dep:

223 1.74±0.33, MG-Repop: 0.62±0.17]), suggesting a strong destabilization of NREMS in the MG-
224 Repop brain (Fig. 2J).
225 During NREMS, brief bursts of brain activity occur at the frequency range of 9-16 Hz, called
226 spindles, which are generated by thalamo-cortical interactions, and play roles in processes such
227 as learning, memory, and cognition [39]. To determine if the lack of MG and its repopulation
228 influence spindle generation, we quantified spindle rate during NREMS episodes and found a
229 significant reduction in MG-Dep mice compared to the control condition (Fig. 2K, L; see
230 "Methods"). However, in contrast to other features of NREMS, MG repopulation normalized the
231 occurrence rate of spindle events, indicating that MG repopulation partially rescued the circuit
232 deficits seen in MG depletion.
233 Altogether, these data suggest that MG is integral part of NREMS establishment and maintenance
234 that might operate in multiple ways like keeping the homeostasis of different neurotransmitters
235 and neuromodulatory connections. Moreover, repopulated postnatal MG fail to settle the normal
236 NREMS regulatory functions of embryo-derived MG.
237
238 **Depletion of microglia prolongs REMS and degrades its quality.**
239 Different neural pathways and neurotransmitters regulate REMS compared to NREMS. However,
240 the role of glial cells and MG in the regulation of REMS is not well understood. We quantified
241 REMS amount across the dark/light periods and found that MG-Dep mice display more REMS
242 compared to the control and MG-Repop conditions during the dark period (Control: 0.67±0.1, MG-
243 Dep: 1.17±0.21 min/h, mean ± SEM). However, in contrast to NREMS, MG repopulation corrected
244 the abnormal expression of REMS (MG-Repop: 0.61±0.13 min/h) (Fig. 3A, B). To investigate if
245 the increase in REMS is due to the consolidation of this state, we performed fragmentation
246 analysis and found that the number of shorter REMS bouts (8 s) is largely decreased (Control:
247 8.7±2.05, MG-Dep: 2.8±1.2, MG-Repop: 8.8±3.3) and longer bouts (>2 min) are increased

248 (Control: 1.5±0.8, MG-Dep: 6.1±1.1, MG-Repop: 4.71±1.4, mean ± SEM) (Fig. 3C), suggesting
249 further stabilization of REMS in the absence of MG.
250 Theta oscillations dominate EEG signal during REMS, where theta phase dynamically modulates
251 gamma amplitude in hippocampal and cortical networks [40]. We next investigated the contribution
252 of MG in theta oscillations and theta-gamma interactions. Spectral analysis of REMS revealed a
253 significant dampening of theta (6-8Hz) power in MG-Dep mice during the baseline dark period
254 (Fig. 3D), which was restored after MG repopulation. We have previously observed REMS
255 stabilization and reduced theta power in mice lacking *Hcrtr*1&2 genes in dorsal raphe serotonergic
256 neurons [38]. We also found that the theta-gamma coupling is significantly reduced in the MG-Dep
257 condition compared to the control. Although MG repopulation attempts to bring it back to the
258 normal level, it fails significantly (Fig. 3E, F). Altogether, these findings suggest that the presence
259 of MG is necessary for the normal expression of REMS, and the local MG that contribute in the
260 generation of REMS and theta oscillations can re-establish large part of their normal function in
261 REMS circuit formations after repopulation.
262 **Microglia contribute to the maintenance of active wakefulness**
263 The quality of prior wakefulness contributes to the expression of both NREMS and REMS. Along
264 these lines, a specific sub-state of prior wakefulness was recently proposed to drive NREMS need
265 [30], and some aspects of wakefulness may functionally substitute for REMS [41]. To investigate how
266 wakefulness is expressed in our experimental conditions, we performed a dynamic analysis of
267 the full waking EEG spectrum across three recording days. This global analysis revealed
268 differential expression of mainly higher waking frequency bands during light-dark cycles across
269 three days, and most notably during enforced wakefulness (SD). As shown in Figure 4a, both
270 MG-Dep and MG-Repop mice exhibit a large dampening of the lower gamma (≈45-55Hz) band
271 during the baseline dark period, which is severely exacerbated during the recovery dark period.
272 Additionally, the MG-Dep mice exhibit a large blunting of the higher gamma band (≈70-90Hz)
273 during SD, which partially normalizes after MG repopulation. However, the lower frequency bands

are not easily distinguishable on the scale of this analysis. We, therefore, performed PSD analysis and found that MG-Dep mice exhibit a large increase in slow delta (1.35-1.75Hz) activity compared to the control mice (Fig. 4B). The increase in this waking frequency band has been previously reported in mice lacking the serotonin transporter gene [38].

Mice spend some portion of their waking time engaged in exploratory and motivated behaviors, such as running, nest building, or drinking, often referred to in rodents as "active wakefulness." These behaviors are associated with the EEG signature called "theta-dominated wakefulness" (TDW 6.0-9.5 Hz), which is highly dependent on the expression of the HCRT neuropeptide, and has been suggested to be the principal driver of the sleep homeostat (Vassalli and Franken, 2017). We quantified TDW in our mice and found a large decrease in its amount in both MG-Dep and MG-Repop mice during the baseline dark period (Fig. 4C, D). This reduction was more pronounced in MG-Repop mice, which was also seen during SD (Fig. 3C, E). TDW is associated with heightened gamma activity. We analyzed the time course of gamma activity during wakefulness and found an increase in slow (32-45Hz) frequency bands in the MG-Repop condition compared to the controls (Fig. 4F). The increase in these frequency bands in MG-Repop mice is quite clear on time-frequency heat maps in Figure 4a.

Overall, these data suggest a significant imbalance in the theta/gamma-rich waking state in both the MG-Dep and MG-Repop conditions, and that there is a heightened gamma activity after MG repopulation.

Disrupted balance of excitatory and inhibitory synaptic signaling and neurotransmitters upon microglial depletion and repopulation

Neurons communicate with each other at synapses, and synaptic plasticity is associated with changes in VS [42]. The expression of synaptic proteins increases during wakefulness and sleep loss and decreases during sleep [43]. Homer1a, a postsynaptic protein and core brain molecular correlate of sleep loss [44], accumulates in neurons during waking period but is excluded from

300 synapses due to high expression of noradrenaline [45]. Microglia play a substantial role in synaptic
301 function, homeostasis, and plasticity in the adult brain. They enhance synaptic activity, prevent
302 hyperexcitability, and maintain brain network synchronization within a physiological range [46-48].
303 These functions are dependent on neuronal activity and VS [49].
304 To investigate whether MG depletion and repopulation induce changes in brain network
305 connectivity at synaptic and neurochemical levels, we analyzed the excitatory and inhibitory
306 synaptic density and metabolite content of the brains of our experimental mice. Using an ImageJ
307 macro, we counted the number of synapses on cortical and hypothalamic neurons (Fig. 5A, B).
308 We found that the number of excitatory Vglut1-Homer1 synapses on NeuN-positive cortical
309 somatosensory neurons was significantly reduced in both MG-Dep and MG-Repop conditions.
310 However, this reduction was more noticeable in MG-Repop mice (Fig. 5C). Interestingly, this
311 effect was regulated at the postsynaptic level rather than the presynaptic level (Fig. 5D, E). We
312 furthermore found that the number of parvalbumin (PV)-originated [50] Synaptotagmin-2-Gephyrin
313 (Syt2-Geph) inhibitory synapses on the cortical somatosensory NeuN neurons was significantly
314 increased under the MG-Repop condition (Fig. 5F, G). This increase could possibly be due to an
315 increase in the activity of PV neurons, as we found that the number of Vglut1-Homer1 excitatory
316 synapses on PV neurons was significantly increased under both MG-Dep and MG-Repop
317 conditions (Fig. 5H, I). Recently, cortical PV neurons have been proposed to be responsible for
318 homeostatic sleep regulation [51]. As the quality of VS largely depends on HCRT signaling [30], we
319 next quantified Vglut1 presynaptic protein synapses that interact with HCRT neurons, based on
320 their colocalization with Homer1 molecules (Fig. 5J). Our findings indicate a significant decrease
321 in the number of Vglut1-Homer1 synapses on hypothalamic HCRT neurons, both in MG-Dep and
322 MG-Repop conditions (Fig. 5K). These results suggest that the function of HCRT neurons may
323 be impaired when MG are depleted from the brain, and that repopulation fails to restore it.
324 To further investigate changes in network connectivity in the brains of MG-Dep and MG-Repop
325 mice, we analyzed additional synaptic markers and specific neurotransmitter receptors on RNA

326 extracted from cortical samples of these mice. Our bulk analysis revealed that some general
327 synaptic markers, such as *Synaptophysin I* (*syp*), are largely downregulated in both experimental
328 mice, while *Slc17a7* and *Homer1* genes are significantly downregulated in the cortex of the MG-
329 Repop condition. Among the specific neurotransmitter markers analyzed, the adrenergic receptor
330 family (e.g. *Adrb2*, *adra2a*, *adrb3*, and *Adra1a*) genes showed a tendency to be less expressed
331 in both MG-Dep and MG-Repop conditions, with a marked decrease in the expression of the
332 *Adra2a* gene. Additionally, we observed a reduction in expression of *cholinergic receptor*
333 *muscarinic 2* (*Chrm2*) and serotonergic receptor *5-Hydroxytryptamine Receptor 1A* (*Htr1a*) genes,
334 which mainly occur in the brain of MG-Repop mice (Fig. 6A).
335 Synapses serve as the junction between pre- and postsynaptic elements in the brain. However,
336 their significance goes far beyond just structural interaction, as they play a crucial role in
337 transmitting neurotransmitters and conveying information that is essential for brain activity. We
338 therefore conducted targeted metabolomics to analyze the neurotransmitter content and
339 metabolite reservoir of the cortex, which is the final functional unit and the region where EEG
340 signals are acquired. This analysis was performed using LC-MS/MS on control, as well as MG-
341 Dep and MG-Repop mice. The purpose of this analysis was to gain a deeper understanding of
342 the changes that might occur in the brain of these mice and how these changes could affect the
343 expression of VS.
344 Our results showed that pharmacological depletion of MG led to a distinct clustering of
345 metabolites, as indicated by the principal component analysis (PCA) (Fig. 6B). This suggests that
346 MG plays an important role in maintaining the overall metabolic composition of the cortex.
347 However, MG repopulation restored the cortical submetabolome to a pattern similar to that
348 observed under control experimental conditions (Figure 6B). Univariate analysis revealed a
349 reduction in norepinephrine upon MG depletion, which was restored after repopulation (Figure
350 6C). The concentrations of acetylcholine, choline, dopamine, and serotonin remained unchanged
351 between the experimental conditions, with a slight tendency to decrease in MG-Dep condition.

352 Furthermore, we observed that MG depletion led to a marked reduction of L-2-amino adipic acid
353 (L-2-AAA), which was only partially recuperated after repopulation (Figure 6C). We also analyzed
354 the precursors of neurotransmitters and found a significant decrease in the amino acids L-serine
355 and asparagine, which could only be partially restored upon MG repopulation (Figure 6D).
356 Similarly, there was a trend towards a decrease in glycine and L-glutamic acid, although not
357 significantly (Figure 6D). These findings indicate substantial alterations in metabolic pathways
358 that play an important role in the regulation of VS.
359 We showed above that the excitatory synaptic input to HCRT neurons was significantly decreased
360 in both MG-Dep and MG-Rep conditions. We therefore quantified the *Hcrt* transcript expression
361 in the hypothalamus of our experimental mice and found a decrease in *Hcrt* expression which
362 was only partially rescued after MG repopulation (Figure 6E). Taken together, our data suggest
363 that while network connectivity is significantly impaired in MG-Dep condition with no restoration
364 after MG repopulation, the underlying substrates (neurotransmitters and metabolites) are largely
365 restored after MG repopulation.
366

367 **Discussion**

368 In this study, we uncovered the reciprocal interaction between VS and brain resident
369 macrophages. While the effects of vigilance states on oligodendrocytes [52] and astrocytes [53] have
370 been documented, their effects on brain resident macrophages are less explored. We
371 demonstrated that lack of sleep induces significant transcriptional changes in both MG and CAMs,
372 and these changes are further amplified when hypothalamic HCRT neurons are ablated.
373 Furthermore, we observed regional differential gene expression in cortical and hypothalamic
374 microglia, which is also impacted by SD. These findings suggest that even a few hours of SD can
375 affect the immune compartments of the brain, potentially influencing their function, such as
376 synaptic elimination [22]. While the transcriptional changes in microglia of HCRT neuron-ablated
377 mice is intriguing, it is crucial to explore the mechanisms through which this neuropeptide
378 influences the biology of these cell types.

379 We also demonstrated that MG depletion has a significant impact on the homeostatic regulation
380 of sleep, and this effect is not fully reversed after MG repopulation. Both NREMS and wakefulness
381 are greatly affected by MG depletion and repopulation, whereas REMS is primarily influenced by
382 MG deficiency, but with significant recovery after MG repopulation. Previous studies have shown
383 that the brain global transcriptomes are little influenced by repopulated microglia [17]. Furthermore,
384 it has been suggested that after MG repopulation, neuroprotection is achieved through IL-6
385 induction in neurons [54]. Other studies demonstrated full functionality of retinal microglia after
386 repopulation, including their role in the continuous surveillance of the retina, behavioral and
387 physiological responses to retinal injury, and maintenance of synaptic structure [55]. However, our
388 data reveal that MG repopulation not only fails to completely restore various aspects of sleep
389 regulation, but in some cases, it exacerbates certain parameters, such as the fragmentation of
390 NREMS and the increase in sleep need. This demomstrates striking funtional differences between
391 microlgial cells derived from pre-or postantal sources. We speculate that not all microglia-
392 neuronal interactions are properly reestablished by adulthood-dervied microglia after

393 repopulation. We observed a significant imbalance between excitatory and inhibitory synapses
394 after depletion of embryo-derived microglia and after repopulation from adult microglia, with a
395 notable increase in inhibitory synapses during repopulation and a significant rise in excitatory
396 synapses interacting with PV inhibitory neurons. Previous studies have suggested that microglia
397 play a role in restraining excessive neuronal activation that cannot be sufficiently suppressed by
398 inhibitory neurons alone [48]. Our results suggest that prenatal microglia also control excessive
399 excitation of inhibitory neurons, but the reasons why this is not corrected with adulthood-derived
400 microglia remain to be investigated.
401 Deficient synaptic neurotransmission was proposed as a potential cause for abnormal sleep
402 regulation [56]. We found here an imbalanced neurotransmitter and metabolite content of the brain
403 in mice devoid of prenatal microglia. It appears that the norepinephrine neurotransmission is
404 particularly sensitive to MG deficiency, as both the levels of norepinephrine metabolites and the
405 corresponding receptors are significantly affected by MG depletion. Norepinephrine is implicated
406 in both wakefulness [21] and sleep regulation [57,58], and it has been suggested that microglial
407 surveillance process relies heavily on norepinephrine signaling [59,60]. Additionally, we observed a
408 decrease in the expression of neurotransmitter precursors such as L-serine, which was mirrored
409 by changes in the concentrations of glycine, asparagine, and glutamic acid. Previous studies have
410 proposed serine as a link between metabolism and neurotransmission [61], and it serves as a
411 precursor for synthesizing ceramide [62], which has been suggested to be essential for maintaining
412 stable wakefulness [35]. Our findings indicate that microglia play a more substantial role in
413 maintaining the physical connectivity of brain networks rather than the neurochemical
414 connectivity, as MG repopulation largely restores metabolites but not synapses. To gain a detailed
415 understanding of microglial regulation of sleep, it is necessary to explore local and specific
416 microglia depletion or disruption of microglia-neuron interactions using inducible systems.
417 Additionally, investigating the separate contributions of microglia and CAMs in sleep regulation
418 using Cre lines under the promoter of *Hexb* [63] and *Mrc1* [64] genes, respectively, would be a starting

point. The observed VS phenotypes may also be influenced by disruptions in other central factors (such as protein phosphorylation orchestrated by microglial TNF-α) [12] and peripheral players (CSF1R inhibition also effects circulating and tissue macrophages) [65] warranting further investigations. Overall, our results shed new light on the complex interaction between the neuroimmune system and sleep regulation, and it paves the way for future investigations in this field.

Data availability

All data are available from the corresponding author upon reasonable request. Bulk RNA sequencing datasets were deposited into the Gene Expression Omnibus database under accession number XXXXX and are available at the following URL: XXXXXXXX.

Acknowledgements

MP was supported by the German Research Foundation (DFG) (TRR167 Project-ID: 259373024, CRC 1479 Project-ID: 441891347, CRC 1160 Project-ID: 256073931, TRR 359 Project-ID: 491676693). MP was further supported by the Novo Nordisk Foundation, the Faber foundation, the Ernst Jung Foundation, the DFG (CRC 992 Project-ID: 192904750, a Reinhart Koselleck grant, the Gottfried Wilhelm Leibniz prize), and the Alzheimer Forschung Initiative e.V. (AFI). This study was further supported by the DFG under Germany's Excellence Strategy (CIBSS, EXC-2189, Project-ID 390939984). MT was supported by Swiss NSF (grant 173126), and the State of Vaud (Faculty of Biology and Medicine, University of Lausanne). AS was supported by Novartis Foundation for medical-biological Research (#23B079).

Author contributions

AS & MP conceptualized and designed the study. AS, MH, SW, VW and LH performed experiments. AS, GM, MB and LH analyzed data. AS, MP, MT, MB, LH and TB wrote the manuscript.

443

444

445 **Declaration of interests**

446 The authors declare no competing interests.

447

448

449 **Methods**

450 **Animals.** Wilde type (C57BL/6) and Hcrt-ataxin-3 transgenic mice were used in this study. All animals were
451 between 12 and 14 weeks old during the time of experiments and animal experiments were approved by
452 the Ministry for Nature, Environment and Consumers` Protection of the state of Baden-Württemberg and
453 were performed in accordance to the respective national, federal, and institutional regulations. At all times,
454 care was taken to minimize animal discomfort and avoid pain.

455

456 **Microglia and CAM isolation and flow cytometry.** Mice brains were collected and microglia were
457 enriched using density gradient separation and were prepared as described previously [66,67]. The cell
458 suspension was then incubated with Fixable Viability Dye eFluor® 780 (1:1000, 65-0865-14, Invitrogen) for
459 10 min at 4 °C. Subsequently, the following antibodies were used: antiCD11b (1:200, clone M1/70, 101235
460 Biolegend), anti-CD45 (1:200, clone 30-F11, 103108 BioLegend), anti-CD11c (1:100, 12-0114-81,
461 Invitrogen), anti-Gr1 (1:200, 108408, Biolegend) and anti-CD206 (1:200, 141708, Biolegend). Cell sorting
462 for RNA-seq was performed on a MoFlo Astrios (Beckman Coulter).

463

464 **Total RNA extraction.** Total RNA was extracted from FACS sorted mouse brain cells stabilized in
465 RNAprotect buffer according to the "Purification of total RNA from animal and human cells" protocol of the
466 RNeasy Plus Micro Kit (QIAGEN, Hilden, Germany).
467 In brief, cells were stored and shipped in buffer RNAprotect at 2-8 °C. After pelleting by centrifugation for 5
468 minutes at 5,000 x g, the RNAprotect was replaced by 350 µl buffer RLT Plus and the samples were
469 homogenized by vortexing for 30 seconds. Genomic DNA contamination was removed by using gDNA
470 Eliminator spin columns. Next one volume of 70 % ethanol was added and the samples were applied to
471 RNeasy MinElute spin columns followed by several wash steps. Finally the total RNA was eluted in 12 µl
472 of nuclease free water. Purity and integrity of the RNA was assessed on the Agilent 2100 Bioanalyzer with
473 the RNA 6000 Pico LabChip reagent set (Agilent, Palo Alto, CA, USA).

474

475 **RNA sequencing.** The SMARTer Ultra Low Input RNA Kit for Sequencing v4 (Clontech Laboratories, Inc.,
476 Mountain View, CA, USA) was used to generate first strand cDNA from approximately 1 ng total-RNA.
477 Double stranded cDNA was amplified by LD PCR (13 cycles) and purified via magnetic bead clean-up.

478 Library preparation was carried out as described in the Illumina Nextera XT Sample Preparation Guide
479 (Illumina, Inc., San Diego, CA, USA). Thereby 150 pg of input cDNA were tagmented (tagged and
480 fragmented) by the Nextera XT transposome. The products were purified and amplified via a limited-cycle
481 PCR program to generate multiplexed sequencing libraries. For the PCR step 1:5 dilutions of the unique
482 dual indexing (i7 and I5) adapters were used. The libraries were quantified using the KAPA Library
483 Quantification Kit - Illumina/ABI Prism User Guide (Roche Sequencing Solutions, Inc., Pleasanton, CA,
484 USA). Equimolar amounts of each library were sequenced on an Illumina NextSeq 2000 instrument
485 controlled by the NextSeq 2000 Control Software (NCS) v1.4.0.39521, using one 50 cycles P3 Flow Cell
486 with the dual index, single-read (SR) run parameters. Image analysis and base calling were done by the
487 Real Time Analysis Software (RTA) v3.9.2. The resulting .cbcl files were converted into .fastq files with the
488 bcl2fastq v2.20 software. RNA extraction, library preparation and RNAseq were performed at the Genomics
489 Core Facility "KFB - Center of Excellence for Fluorescent Bioanalytics" (University of Regensburg,
490 Regensburg, Germany; www.kfb-regensburg.de). Bulk RNA-seq data was aligned with STAR v2.7.10a [68]
491 to the mouse reference genome Gencode M26 [69]. Counts were obtained from the bam files with the tool
492 featureCounts v2.0.3. Genes with count expression higher than 5 in at least 3 samples were kept for the
493 differential expression analysis. Differential expression was performed using the limma trend method [70] on
494 the log2 counts per million (CPM) values. Venn diagrams and Volcano plots were generated with the R
495 packages limma and EnhancedVolcano, respectively. Enrichment analysis was performed using ShinyGO
496 [71].
497
498 **Gene expression analysis.** For qPCR analysis, RNA extracted from the cortical samples of control, MG-
499 Dep and MG-Repop mice. RNA was extracted using RNeasy micro kit (74004) and cDNA synthesis was
500 performed using random hexamer primers and M-MLV Reverse Transcriptase Promega kit (M3682). SYBR
501 green-based and Taqman probes were used to detect the gene expression. The assay was performed
502 using a LightCycler480 (Roche).
503
504 **Immunofluorescence and synapse counting**. Mice were anesthetized with ketamine (100mg per kg body
505 weight) and xylazine (10mg per kg body weight) followed by perfusion with 1× PBS. For histology, brains
506 were kept overnight in 4% paraformaldehyde (PFA). Brains were then dehydrated in 30% sucrose for about
507 48 hours and then snap-frozen on dry ice. Cryosections (14µm for synapse counting and 20µm for microglia
508 and CAM staining) from brain tissue were prepared as free floating in PBS. The following antibodies were
509 used to stain microglia, CAM and synapses: Rabbit-anti-Iba1 (ab178846, abcam), Rat-anti-CD206 (Biorad
510 MCA2235), Goat-anti-Collagene type 4 (Millipore AB769), anti-NeuN (ab177487, ab104224, abcam), anti-
511 Vglut1 (135304, synaptic system), anti-Homer1 (ABN37, Millipore), anti-Gephyrin (147318, synaptic
512 system), anti-Synaptotagmin-2 (ZDB-ATB-081002-25, ZFIN), anti-Parvalbumin (MAB1572, Merck) and
513 anti-Hcrt-A (SC-8070). The DAPI was used to stain the nucleus. Rat-anti-CD206 and Goat-anti-Collagene
514 type 4 antibodies were incubated for 48 hours at 4 °C to have high quality staining. Iba1 antibody was

515 incubated overnight at 4 °C and the primary antibodies to detect synapses were incubated for 1.45hr at
516 room temperature. The brain cuts were incubated with secondary antibodies for 1-2 hours at room
517 temperature. Fluorescence imaging was performed with TCS SP8 X (Leica Microsystems). Imaging of
518 synapses was performed using 63X objective with zoom factor 8. Iba1^{+} cells were counted using Fiji.
519 Synapse analysis and quantification were conducted using Fiji macro developed previously [72] with little
520 modifications.
521
522 **Quantitative profiling of metabolites by liquid chromatography and mass spectrometry (LC-MS/MS).**
523 Mice brain tissue biopsies were thawed and homogenised with ice-cold PBS supplemented with 1%
524 protease inhibitor cocktail (Sigma Nr. P8340-5ML), using a cordless pestle motor and disposable pellet
525 mixers (VWR Nr. 47747-366). Buffer volume was adjusted to reach a target of 0.1 to 0.3 mg wet-tissue/mL
526 lysis buffer. Whole tissue homogenates were aliquoted for downstream measurement of total protein
527 concentration, flash-frozen and stored at -80 ºC. Sulfur-containing metabolites as well as creatinine, S-
528 adenosylmethionine and S-adenosylhomocysteine were determined according to a previously published
529 procedure [73,74]. Lactate, TCA and glycolysis intermediates and other organic acids, and folates were
530 determined as described in previous work [75]. Amino acids and neurotransmitters were determined using a
531 previously described protocol [76,77]. A commercially available standardized amino acid mixture was utilized
532 to generate a calibration curve for amino acids (Amino acid standards, physiological, Sigma, Nr. A9906-
533 10ML). Calibration curves for all other metabolites were prepared from individual stock solutions prepared
534 in house. Quantitation accuracy was examined by monitoring homocysteine and methylmalonic acid
535 concentrations in an external quality control, namely, the Control Special Assays in Serum, European
536 Research Network for the evaluation and improvement of screening, diagnosis, and treatment of Inherited
537 disorders of Metabolism (ERNDIM) IQCS, SAS-02.1 and SAS-02.2 from MCA Laboratories, Winterswijk,
538 Netherlands. For all other metabolites, quantitation trueness was tested by examining metabolite
539 concentrations in plasma from a previously validated sample isolated from a healthy control individual with
540 respect to standard reference ranges, using the same calibration curves and LC-MS/MS running conditions.
541 Quantification of metabolites was carried out with Analyst® 1.7.2 software, 2022 AB Sciex.
542
543 **Treatments.** In order to eliminate cells dependent on CSF1R (MG) mice were administered a CSF1R
544 inhibitor called PLX5622 (Plexxikon). The inhibitor was combined with AIN-76A standard chow at a
545 concentration of 1,200ppm (Research Diets) and the mice were given unrestricted access to it for two
546 weeks. The control group received AIN-76A standard chow without any modifications. After two weeks the
547 PLX5622 food was replaced with control food to start repopulation of MG.
548
549 **Mice surgery, data acquisition and vigilance state analysis.** Mice surgery and data acquisition were
550 performed as previously described [38]. MATLAB scripts were created to quantify various parameters related
551 to wakefulness, NREMS and REMS. These parameters include time distribution and amount of episodes,

552 as well as the fragmentation of vigilance states, all of which were defined based on previously established
553 criteria [38]. TDW analysis was conducted following the method described by Vassalli and Franken [30].
554
555 **Power spectral analysis.** Using Somnologica-3TM (Medcare) software, each 4 s epoch of the EEG signal
556 was subjected to discrete Fourier transform to determine EEG power density (spectra 0–90 Hz at a
557 frequency resolution of 0.25 Hz). We used artifact-free, same-state–flanked 4 s epochs to calculate the
558 mean EEG spectral profiles for each behavioral states and time intervals. To account for differences among
559 animals in absolute EEG power, the mean values of spectral profiles were converted into percentages
560 relative to a baseline EEG power reference value of 100%. This reference value was determined for each
561 mouse by summing the power within the frequency range of 0.75–47.5 Hz across all states and throughout
562 the first day of baseline recordings. To control for differences in the amount of wakefulness, NREMS and
563 REMS, this reference was weighted so that the relative contribution of each state was identical for all mice
564 [78]. Time-frequency heatmaps of EEG power during wakefulness were generated using methods described
565 previously [79].
566
567 **Time-course analysis.** In order to examine the dynamic changes of EEG power within specific frequency
568 ranges throughout the day and night, the time-course of the activity of that frequency band was computed
569 for 4 s epochs scored as state of interest (NREMS, REMS and wake). For this purpose, the epochs for
570 each state were divided into percentiles, ensuring that each percentile contained a roughly equal number
571 of epochs. The number of percentiles for NREMS and REMS were: 12 for light periods, 6 for dark periods,
572 and 8 for the 6-h light period after SD; for waking state: 6 for light periods, 12 for dark periods, 8 for the 6-
573 h light SD, and 4 for the 6-h light after SD. The average EEG power within the specified frequency range
574 was computed for each percentile, and subsequently normalized based on the type of analysis. This
575 normalization was either done relative to the total power of the baseline state or with respect to the power
576 achieved within the delta frequency band during slow-wave sleep at ZT8-12. Like power density analysis,
577 single epochs were excluded and only power values of the epochs that themselves, as well as the two
578 adjacent ones, were scored as artifact-free same-state were included in the analysis.
579
580 **Theta-gamma cross-frequency coupling.** We used the modulation index (MI) to measure the theta-
581 gamma phase-amplitude coupling [40,80]. Using finite impulse response filters with an order equal to three
582 cycles of the low cutoff frequency, we first bandpass-filtered EEG signals into theta (6-11 Hz) and fast-
583 gamma (54-90 Hz) in both forward and reverse directions to eliminate phase distortion. We then estimated
584 instantaneous phase of theta and the envelope of fast-gamma using the Hilbert transform. Theta phase
585 was discretized into 18 equal bins (N=18, each 20°) and the average value of fast-gamma envelope within
586 each bin was calculated. The resulting phase-amplitude histogram (P) was compared with a uniform
587 distribution (U) using the Kullback-Leibler distance, $D_{KL}(P,U) = \sum_{j=1}^{N} P(j) * log[P(j)/U(j)]$, and normalized
588 by $log(N)$ to obtain the modulation index, $MI = D_{KL} / log(N)$. To explore possible coupling patterns between

different pairs of low and high frequency bands, we used the comodulogram analysis [80]. We considered 16 frequency bands for phase (1-18 Hz, 1-Hz increments, 2-Hz bandwidth), and 14 frequency bands for amplitude (15-90 Hz, 5-Hz increments, 10-Hz bandwidth). MI values were then calculated for all these pairs to obtain the comodulogram graph.

Detection of sleep spindles. NREMS spindles were detected automatically using an optimized wavelet-based method as previously described [39]. Briefly, the power of EEG signals within 9-16Hz was estimated using the complex B-spline wavelet function, and smoothed using a 200 ms Hanning window, and then a threshold equal to 3 SD (SD: standard deviation) above the mean was applied to detect the potential spindle events. Events shorter than 400 ms or longer than 2 s were discarded. Using band pass-filtered EEG signals in the spindle range (9–16 Hz), we automatically counted the number of cycles of each detected event and excluded those with <5 cycles or more than 30 cycles. To discard artefacts, events with a power in the spindle band lower than 6–8.5 Hz or 16.5–20 Hz power bands were not included.

Statistical analysis. The specific number (n) of replicates employed in each experiment is provided in the corresponding figure legends. The individuals responsible for conducting SD and scoring the sleep recordings were unaware of the genotype of the animals, ensuring blinding during these procedures. The results are presented as mean ± SEM or mean ± SD. Statistical analyses were conducted using GraphPad Prism. The significance of comparisons was determined using one- or two-way ANOVA or mix effect model followed by relevant post hoc tests and are reported in the figure legends.

614 **Figure legends**

615

616 **Figure 1. Large transcriptional changes in the hypothalamic and cortical microglia and**
617 **CAMs of WT and Ataxin mice after six hours of SD.** (**A**) (left) parenchymal Iba1$^+$ cells
618 (microglia) in green and perivascular space (yellow arrowheads) and meningeal (white
619 arrowheads) Iba1$^+$ cells (CAMs) in red. CAMs are positive for CD206 protein expression and are
620 found in the collagen (Col) IV$^+$ perivascular compartment (right). (**B**) CD11b$^+$; CD45Intermediate
621 microglia were sorted separately from the cortex and hypothalamus of WT and Ataxin mice.
622 CD11b and CD206 positive CAMs were sorted from the whole brain of the both genotypes. (**C**)
623 heatmap showing differentially expressed genes in microglia from hypothalamus and cortex of
624 WT mice under SD and control conditions. Each column represents microglia gene expression
625 from one individual mouse, with 4-5 mice per group. Color code represents linear scale. (**D**)
626 heatmap showing differentially expressed genes in microglia from hypothalamus and cortex of
627 Ataxin mice under SD and control conditions. (**E**) Volcano plots depicting differentially regulated
628 cortical and hypothalamic microglial genes between the SD and control groups in WT mice.
629 NS = not significant. (**F**) Venn diagram depicting the number of differentially regulated and
630 overlapping genes between microglia of WT and Ataxin mice. Red and dark blue represents up
631 and downregulated genes respectively. (**G**, **H**, **I** and **J**) Radar plots representing DEGs in microglia
632 of cortex (Cx) and hypothalamus (Hy) in WT (green dots) and Ataxin (blue dots) mice under SD
633 (white, upper part) and control (noSD) condition (yellow, bottom). (**K**) Volcano plots depicting
634 differentially regulated CAMs genes between the SD and control groups in WT mice. NS = not
635 significant. (**L**) Bar plots showing the expression of *App* and *Lyve-1* genes under the SD and
636 control conditions in CAMs of WT mice. Values are presented as mean ± SEM, n =4-5 (t-test, *P
637 < 0.05; **P < 0.01; ***P < 0.001). (**M**) Volcano plots depicting differentially regulated CAMs genes
638 between the SD and control groups in Ataxin mice.

639

640 **Figure 2. MG are essential for the proper regulation of NREMS.** (**A**) Schematic figure
641 illustrating the experimental procedure conducted on adult mice to assess the brain's electrical
642 activity using EEG. Prior to drug administration, the first recordings were obtained. These initial
643 recordings served as controls. Subsequently, the mice were fed food containing PLX5622 for a
644 duration of two weeks. The second recording was conducted during the final three days of this
645 period. Following the drug treatment, the mice were once again provided with control food. Upon
646 completion of this phase, the third recording was performed. (**B, C**) PLX5622 substantially
647 depletes the microglia from the brain, and removing it brings the microglia back to the brain. (**D**)

Recording paradigm. The first two days of recordings served as baseline, and were averaged and represented as one day. The second day consisted of 6 hours of SD and 18 hours of recovery. (**E**) Time-course of vigilance states; Wakefulness (top) and NREMS (bottom). MG-Dep and –Repop mice show a large increase in NREMS amount during the dark period both at baseline and during recovery (n = 9 for control and MG-Depleted conditions and n = 6 for MG-Repopulated condition, two-way ANOVA, followed by Dunnett's test, *P < 0.05; **P < 0.01; ***P < 0.001, orange and blue stars are significant differences between control mice and MG-Dep and MG-Repop mice respectively). Data points are shown in minutes per hour (min/h) and represent the average of 2 h. (**F**) From left to right: the total amount of wakefulness (top) and NREMS (bottom) during baseline light, dark and recovery light and dark periods (Mixed-effects analysis, followed by Dunnett's test, *P < 0.05; **P < 0.01; ***P < 0.001). (**G**) Time-course of the EEG delta power (1–4 Hz) in the course of the 3-day recording. EEG delta power denotes sleep need. As shown, both MG-Repop and MG-Dep animals have deficiency to build up sleep need during dark period (two-way ANOVA, followed by Dunnett's test, *P < 0.05; **P < 0.01; ***P < 0.001, orange and blue stars are significant differences between control mice and MG-Dep and MG-Repop mice respectively). (**H**) EEG power spectra of all experimental mice in NREMS during baseline light (left) and dark (right) periods. Insets indicate amplification for specific EEG frequencies (two-way ANOVA, followed by Dunnett's test, *P < 0.05; **P < 0.01; ***P < 0.001, orange and blue stars are significant differences between control mice and MG-Depleted and MG-Repopulated mice respectively). (**I**) EEG power spectra of all experimental mice in NREMS during recovery light (left) and dark (right) periods. (**J**) Distribution of NREMS bout durations during baseline dark period across three experimental mice. Sleep bout length are presented on the x-axis (one-way ANOVA, followed by Tukey test). (**K**) (Top) Heatmap showing the average time–frequency representations of spindles. (Bottom) Representative EEG/EMG signals of a detected spindle. The dashed horizontal lines indicate upper and lower thresholds to detect the spindle using the wavelet energy within 9-16 Hz, and the dashed vertical lines indicate the start and the end of the detected spindle. (**L**) Spindle rate during NREMS episodes of different conditions. Spindle rate significantly decreased in MG-depleted mice (Mixed-effects analysis, followed by Dunnett's test, *P < 0.05; **P < 0.01; ***P < 0.001)).

Figure 3. REMS regulation largely depends on the presence of the microglia. (**A**) Time-course of distribution of REMS amount across three conditions. MG-Dep mice exhibit a large increase in REMs amount during the baseline dark period (n = 9 for control and MG-Dep conditions and n = 6 for MG-Repop condition, two-way ANOVA, followed by Dunnett's test, *P <

682 0.05; **P < 0.01; ***P < 0.001, orange and blue stars are significant differences between control
683 mice and MG-Dep and MG-Repop mice respectively). Data points are shown in minutes per hour
684 (min/h) and represent the average of 2 h. (**B**) Total amount of REMS during baseline dark period
685 (Mixed-effects analysis, followed by Dunnett's test, *P < 0.05; **P < 0.01; ***P < 0.001). (**C**)
686 Distribution of REMs bout durations during baseline dark period across three experimental mice.
687 Sleep bout length are presented on the x-axis (one-way ANOVA, followed by Tukey test). (**D**)
688 EEG power spectra of all experimental mice in REMS during baseline dark period. Insets indicate
689 amplification for specific EEG frequencies (two-way ANOVA, followed by Dunnett's test, *P <
690 0.05; **P < 0.01; ***P < 0.001, orange and blue stars are significant differences between control
691 mice and MG-Dep and MG-Repop mice respectively). (**E**) Comodulogram graphs show the
692 modulation index for a wide range of frequency pairs, obtained from 12-h recordings of one animal
693 in different conditions. (**F**) Normalized theta-gamma coupling across three experimental
694 conditions. Theta-gamma coupling is significantly decreased in MG-depleted and -repopulated
695 conditions (Mixed-effects analysis, followed by Dunnett's test, *P < 0.05; **P < 0.01; ***P <
696 0.001)).
697 .
698
699 **Figure 4. MG Repopulation fails to normalize the waking state deficits observed under the**
700 **MG Depleted condition.** (**A**) Heatmaps of time x frequency x power representations of the waking
701 EEG of control, MG-Dep and MG-Repop mice across the 3 recorded days (48h baseline, a 6h
702 sleep deprivation and 18h recovery) show large changes in higher frequency bands. (**B**) EEG
703 power spectra of all experimental mice in wakefulness during baseline light and dark periods (two-
704 way ANOVA, followed by Dunnett's test, *P < 0.05; **P < 0.01; ***P < 0.001, orange star are
705 significant differences between control mice and MG-Dep mice). (**C**) Time-course distribution of
706 TDW amounts indicates decreased amount during the dark period in MG-Dep and MG-Rep. Data
707 points are shown in minutes/hour and represent the average of 2 hours (baselines are averaged),
708 (two-way ANOVA followed by Dunnett's test, orange and blue stars are significant differences
709 between control mice and MG-Dep and MG-Repop mice respectively). (**D**) Quantification of total
710 amount of TDW during baseline light and dark period (Mixed-effects analysis, followed by
711 Dunnett's test, *P < 0.05; **P < 0.01; ***P < 0.001). (**E**) Total amount of TDW during SD. (**F**)
712 Waking EEG slow-gamma (32-45 Hz) power dynamics in the course of the 3-day recording
713 (baseline one and two are averaged) (two-way ANOVA, followed by Dunnett's test).
714

715 **Figure 5. Large synaptic imbalance after MG depletion and Repopulation in the cortex and**
716 **hypothalamus.** (**A**) Schematic figure depicting the cell types on which the number of synapses
717 was counted. NeuN (blue) and PV (orange) positive neurons in the cortex and Hcrt neurons in
718 the hypothalamus. The number of the co-localized excitatory Vglut1 – Homer1 synaptic proteins
719 on NeuN, PV and Hcrt positive neurons were counted. Additionally, the number of the inhibitory
720 Syt2-Gephyrin synaptic proteins on NeuN neurons were counted. (**B**) Representative image
721 depicting pre, postsynaptic proteins and their colocalization with NeuN positive neurons. The
722 synapses are shown with arrowheads and marked with pink color by ImageJ macro (right). Scale
723 bar: 10μm. (**C**) number of vGlut1-Homer1 synapses/μm2 of NeuN+ soma. N=342 cell from 12
724 mice for control, 324 cell from 11 mice for MG-Dep and 357 cell from 12 mice for MG-Repop
725 conditions. The results show reduced number of these synapses in both MG-Dep and MG-Repop
726 conditions (**D**) Number of Homer1 puncta/μm2 of NeuN+ soma. (**E**) Number of Vglut1 puncta/μm2
727 of NeuN+ soma. (**F**) Number of Syt2-Gephyrin synapses/μm2 of NeuN+ soma. N=299 cell from
728 12 mice for control, 270 cell from 11 mice for MG-Dep and 306 cell from 12 mice for MG-Repop
729 conditions. (**G**) Syt2-Gephyrin synapses on NeuN positive cortical neuron. Large increase in this
730 inhibitory is observed under MG-Repop condition. Scale bar: 10μm. (**H**) distribution of the PV
731 positive neurons in the cortex. Scale bar: 100 and 10 μm. (**I**) Number of vGlut1-Homer1
732 synapses/μm2 of PV+ soma. N=29 cell from 5 mice for control, 29 cell from 5 mice for MG-Dep
733 and 23 cell from 4 mice for MG-Repop conditions. (**J**) Hcrt neurons distribution in the lateral
734 hypothalamus. Red: Hcrt neuron, green (Vglut1) and Cyan (Homer1). Scale bar: 100 and 10 μm.
735 (**K**) number of vGlut1-Homer1 synapses/μm2 of Hcrt+ soma. N=70 cell from 3 mice for control,
736 73 cell from 3 mice for MG-Dep and 77 cell from 4 mice for MG-Repop conditions. One-way
737 ANOVA, followed by Dunnett's test, *P < 0.05; **P < 0.01; ***P < 0.001.
738
739 **Figure 6. Significant changes occur in neurotransmitter receptors and metabolite content**
740 **following MG depletion and Repopulation.** (**A**) Gene expression level of synaptic proteins and
741 neurotransmitter receptors at RNA level following MG depletion and Repopulation. N=3 for control
742 and MG-Dep and n=4 for MG-Repop conditions. One-way ANOVA, followed by Tukey test, *P <
743 0.05; **P < 0.01; ***P < 0.001. (**B**) PCA on targeted metabolites of cortex isolated from control
744 (n=3), MG depleted (n=3) and Repopulated (n=4) animals. (**C**) LC-MS/MS measured
745 neurotransmitter content in the brain of control, MG-Dep and MG-Repop mice. (**D**) Down
746 regulation of amino acids in the brain of experimental mice. (**E**) QPCR analysis of the *Hcrt* gene
747 expression in the hypothalamus of the control, MG-Dep and MG-Repop mice.
748

749 **Figure S1: Transcriptional Changes in Microglial core genes after SD.** (**A**) Bar plots showing
750 the expression of microglial core genes in the cortex and hypothalamus under SD and NoSD
751 (control) conditions. The color codes are provided. (**B**) Bar plots showing the expression of *Lyz2*
752 and *Slc31a2* genes. (**C**) Bar plots showing the expression of the *Adrb2* gene. *P < 0.05; **P <
753 0.01; ***P < 0.001.

754 **Figure S2: Region and genotype specific transcriptional changes in microglial genes after**
755 **SD.**

756 Heatmap showing differentially expressed genes in microglia of the cortex and hypothalamus in
757 WT and Ataxin mice under SD and control conditions. Each column represents microglia data
758 from one individual mouse, with 4-5 mice per group. The color code represents a linear scale.

759 **Figure S3: Gene set enrichment analysis for DEGs of microglia and CAM in WT and Ataxin**
760 **mice.**

761 (**A**) Gene set enrichment analysis for DEGs in microglia of WT and Ataxin mice (**B**), as well as
762 CAMs of WT mice (**C**).

763

764 ## References

765 1 Amann, L., Masuda, T. & Prinz, M. Mechanisms of myeloid cell entry to the healthy and diseased
766 central nervous system. *Nature immunology* **24**, 393-407 (2023).
767 https://doi.org:10.1038/s41590-022-01415-8
768 2 Kierdorf, K., Masuda, T., Jordão, M. J. C. & Prinz, M. Macrophages at CNS interfaces: ontogeny
769 and function in health and disease. *Nature reviews. Neuroscience* **20**, 547-562 (2019).
770 https://doi.org:10.1038/s41583-019-0201-x
771 3 Prinz, M., Masuda, T., Wheeler, M. A. & Quintana, F. J. Microglia and Central Nervous System-
772 Associated Macrophages-From Origin to Disease Modulation. *Annual review of immunology* **39**,
773 251-277 (2021). https://doi.org:10.1146/annurev-immunol-093019-110159
774 4 Sankowski, R. *et al.* Multiomic spatial landscape of innate immune cells at human central
775 nervous system borders. *Nat Med* (2023). https://doi.org:10.1038/s41591-023-02673-1
776 5 Prinz, M., Jung, S. & Priller, J. Microglia Biology: One Century of Evolving Concepts. *Cell* **179**, 292-
777 311 (2019). https://doi.org:10.1016/j.cell.2019.08.053
778 6 Paolicelli, R. C. *et al.* Synaptic pruning by microglia is necessary for normal brain development.
779 *Science (New York, N.Y.)* **333**, 1456-1458 (2011). https://doi.org:10.1126/science.1202529
780 7 Chen, Z. *et al.* Microglial displacement of inhibitory synapses provides neuroprotection in the
781 adult brain. *Nature communications* **5**, 4486 (2014). https://doi.org:10.1038/ncomms5486
782 8 Tansley, S. *et al.* Microglia-mediated degradation of perineuronal nets promotes pain. *Science*
783 *(New York, N.Y.)* **377**, 80-86 (2022). https://doi.org:10.1126/science.abl6773
784 9 Kohno, K. *et al.* A spinal microglia population involved in remitting and relapsing neuropathic
785 pain. *Science (New York, N.Y.)* **376**, 86-90 (2022). https://doi.org:10.1126/science.abf6805
786 10 Cornell, J., Salinas, S., Huang, H. Y. & Zhou, M. Microglia regulation of synaptic plasticity and
787 learning and memory. *Neural regeneration research* **17**, 705-716 (2022).
788 https://doi.org:10.4103/1673-5374.322423
789 11 Shigemoto-Mogami, Y., Hoshikawa, K., Goldman, J. E., Sekino, Y. & Sato, K. Microglia enhance
790 neurogenesis and oligodendrogenesis in the early postnatal subventricular zone. *The Journal of*
791 *neuroscience : the official journal of the Society for Neuroscience* **34**, 2231-2243 (2014).
792 https://doi.org:10.1523/jneurosci.1619-13.2014
793 12 Pinto, M. J. *et al.* Microglial TNFα orchestrates protein phosphorylation in the cortex during the
794 sleep period and controls homeostatic sleep. *The EMBO journal* **42**, e111485 (2023).
795 https://doi.org:10.15252/embj.2022111485
796 13 Kierdorf, K. *et al.* Microglia emerge from erythromyeloid precursors via Pu.1- and Irf8-
797 dependent pathways. *Nature neuroscience* **16**, 273-280 (2013). https://doi.org:10.1038/nn.3318
798 14 Schulz, C. *et al.* A lineage of myeloid cells independent of Myb and hematopoietic stem cells.
799 *Science (New York, N.Y.)* **336**, 86-90 (2012). https://doi.org:10.1126/science.1219179
800 15 Bruttger, J. *et al.* Genetic Cell Ablation Reveals Clusters of Local Self-Renewing Microglia in the
801 Mammalian Central Nervous System. *Immunity* **43**, 92-106 (2015).
802 https://doi.org:10.1016/j.immuni.2015.06.012
803 16 Tay, T. L. *et al.* A new fate mapping system reveals context-dependent random or clonal
804 expansion of microglia. *Nature neuroscience* **20**, 793-803 (2017).
805 https://doi.org:10.1038/nn.4547
806 17 Huang, Y. *et al.* Repopulated microglia are solely derived from the proliferation of residual
807 microglia after acute depletion. *Nature neuroscience* **21**, 530-540 (2018).
808 https://doi.org:10.1038/s41593-018-0090-8

18 Ramar, K. *et al.* Sleep is essential to health: an American Academy of Sleep Medicine position statement. *Journal of clinical sleep medicine : JCSM : official publication of the American Academy of Sleep Medicine* **17**, 2115-2119 (2021). https://doi.org:10.5664/jcsm.9476

19 Irwin, M. R. & Vitiello, M. V. Implications of sleep disturbance and inflammation for Alzheimer's disease dementia. *The Lancet. Neurology* **18**, 296-306 (2019). https://doi.org:10.1016/s1474-4422(18)30450-2

20 Saper, C. B., Chou, T. C. & Scammell, T. E. The sleep switch: hypothalamic control of sleep and wakefulness. *Trends Neurosci* **24**, 726-731 (2001). https://doi.org:10.1016/s0166-2236(00)02002-6

21 Seifinejad, A., Vassalli, A. & Tafti, M. Neurobiology of cataplexy. *Sleep Med Rev* **60**, 101546 (2021). https://doi.org:10.1016/j.smrv.2021.101546

22 Choudhury, M. E. *et al.* Phagocytic elimination of synapses by microglia during sleep. *Glia* **68**, 44-59 (2020). https://doi.org:10.1002/glia.23698

23 Corsi, G. *et al.* Microglia modulate hippocampal synaptic transmission and sleep duration along the light/dark cycle. *Glia* **70**, 89-105 (2022). https://doi.org:10.1002/glia.24090

24 Ingiosi, A. M., Opp, M. R. & Krueger, J. M. Sleep and immune function: glial contributions and consequences of aging. *Current opinion in neurobiology* **23**, 806-811 (2013). https://doi.org:10.1016/j.conb.2013.02.003

25 Tafti, M. *et al.* Major histocompatibility class II molecules in the CNS: increased microglial expression at the onset of narcolepsy in canine model. *The Journal of neuroscience : the official journal of the Society for Neuroscience* **16**, 4588-4595 (1996). https://doi.org:10.1523/jneurosci.16-15-04588.1996

26 Tuan, L. H. & Lee, L. J. Microglia-mediated synaptic pruning is impaired in sleep-deprived adolescent mice. *Neurobiology of disease* **130**, 104517 (2019). https://doi.org:10.1016/j.nbd.2019.104517

27 Bellesi, M. *et al.* Sleep Loss Promotes Astrocytic Phagocytosis and Microglial Activation in Mouse Cerebral Cortex. *The Journal of neuroscience : the official journal of the Society for Neuroscience* **37**, 5263-5273 (2017). https://doi.org:10.1523/jneurosci.3981-16.2017

28 Hara, J. *et al.* Genetic ablation of orexin neurons in mice results in narcolepsy, hypophagia, and obesity. *Neuron* **30**, 345-354 (2001). https://doi.org:10.1016/s0896-6273(01)00293-8

29 Adamantidis, A. R., Zhang, F., Aravanis, A. M., Deisseroth, K. & de Lecea, L. Neural substrates of awakening probed with optogenetic control of hypocretin neurons. *Nature* **450**, 420-424 (2007). https://doi.org:10.1038/nature06310

30 Vassalli, A. & Franken, P. Hypocretin (orexin) is critical in sustaining theta/gamma-rich waking behaviors that drive sleep need. *Proceedings of the National Academy of Sciences of the United States of America* **114**, E5464-e5473 (2017). https://doi.org:10.1073/pnas.1700983114

31 Dauvilliers, Y. *et al.* Post-H1N1 narcolepsy-cataplexy. *Sleep* **33**, 1428-1430 (2010). https://doi.org:10.1093/sleep/33.11.1428

32 Drieu, A. *et al.* Parenchymal border macrophages regulate the flow dynamics of the cerebrospinal fluid. *Nature* **611**, 585-593 (2022). https://doi.org:10.1038/s41586-022-05397-3

33 Zhang, Y. W., Thompson, R., Zhang, H. & Xu, H. APP processing in Alzheimer's disease. *Molecular brain* **4**, 3 (2011). https://doi.org:10.1186/1756-6606-4-3

34 Roh, J. H. *et al.* Potential role of orexin and sleep modulation in the pathogenesis of Alzheimer's disease. *The Journal of experimental medicine* **211**, 2487-2496 (2014). https://doi.org:10.1084/jem.20141788

35 Liu, H. *et al.* Microglia modulate stable wakefulness via the thalamic reticular nucleus in mice. *Nature communications* **12**, 4646 (2021). https://doi.org:10.1038/s41467-021-24915-x

36 Dagher, N. N. *et al.* Colony-stimulating factor 1 receptor inhibition prevents microglial plaque association and improves cognition in 3xTg-AD mice. *Journal of neuroinflammation* **12**, 139 (2015). https://doi.org:10.1186/s12974-015-0366-9

37 Van Hove, H. *et al.* A single-cell atlas of mouse brain macrophages reveals unique transcriptional identities shaped by ontogeny and tissue environment. *Nature neuroscience* **22**, 1021-1035 (2019). https://doi.org:10.1038/s41593-019-0393-4

38 Seifinejad, A., Li, S., Possovre, M. L., Vassalli, A. & Tafti, M. Hypocretinergic interactions with the serotonergic system regulate REM sleep and cataplexy. *Nat Commun* **11**, 6034 (2020). https://doi.org:10.1038/s41467-020-19862-y

39 Bandarabadi, M. *et al.* A role for spindles in the onset of rapid eye movement sleep. *Nature communications* **11**, 5247 (2020). https://doi.org:10.1038/s41467-020-19076-2

40 Bandarabadi, M. *et al.* Dynamic modulation of theta-gamma coupling during rapid eye movement sleep. *Sleep* **42**, 1-11 (2019). https://doi.org:10.1093/sleep/zsz182

41 Endo, T. *et al.* Selective REM sleep deprivation in humans: effects on sleep and sleep EEG. *The American journal of physiology* **274**, R1186-1194 (1998). https://doi.org:10.1152/ajpregu.1998.274.4.R1186

42 Tononi, G. & Cirelli, C. Sleep and synaptic homeostasis: a hypothesis. *Brain research bulletin* **62**, 143-150 (2003). https://doi.org:10.1016/j.brainresbull.2003.09.004

43 Gilestro, G. F., Tononi, G. & Cirelli, C. Widespread changes in synaptic markers as a function of sleep and wakefulness in Drosophila. *Science (New York, N.Y.)* **324**, 109-112 (2009). https://doi.org:10.1126/science.1166673

44 Maret, S. *et al.* Homer1a is a core brain molecular correlate of sleep loss. *Proceedings of the National Academy of Sciences of the United States of America* **104**, 20090-20095 (2007). https://doi.org:10.1073/pnas.0710131104

45 Diering, G. H. *et al.* Homer1a drives homeostatic scaling-down of excitatory synapses during sleep. *Science (New York, N.Y.)* **355**, 511-515 (2017). https://doi.org:10.1126/science.aai8355

46 Merlini, M. *et al.* Microglial G(i)-dependent dynamics regulate brain network hyperexcitability. *Nature neuroscience* **24**, 19-23 (2021). https://doi.org:10.1038/s41593-020-00756-7

47 Akiyoshi, R. *et al.* Microglia Enhance Synapse Activity to Promote Local Network Synchronization. *eNeuro* **5** (2018). https://doi.org:10.1523/eneuro.0088-18.2018

48 Badimon, A. *et al.* Negative feedback control of neuronal activity by microglia. *Nature* **586**, 417-423 (2020). https://doi.org:10.1038/s41586-020-2777-8

49 Hristovska, I. *et al.* Sleep decreases neuronal activity control of microglial dynamics in mice. *Nature communications* **13**, 6273 (2022). https://doi.org:10.1038/s41467-022-34035-9

50 Bouhours, B., Gjoni, E., Kochubey, O. & Schneggenburger, R. Synaptotagmin2 (Syt2) Drives Fast Release Redundantly with Syt1 at the Output Synapses of Parvalbumin-Expressing Inhibitory Neurons. *The Journal of neuroscience : the official journal of the Society for Neuroscience* **37**, 4604-4617 (2017). https://doi.org:10.1523/jneurosci.3736-16.2017

51 Kon, K. *et al.* Cortical parvalbumin neurons are responsible for homeostatic sleep rebound through CaMKII activation. *bioRxiv*, 2023.2004.2029.537929 (2023). https://doi.org:10.1101/2023.04.29.537929

52 Bellesi, M. *et al.* Effects of sleep and wake on oligodendrocytes and their precursors. *The Journal of neuroscience : the official journal of the Society for Neuroscience* **33**, 14288-14300 (2013). https://doi.org:10.1523/jneurosci.5102-12.2013

53 Bellesi, M., de Vivo, L., Tononi, G. & Cirelli, C. Effects of sleep and wake on astrocytes: clues from molecular and ultrastructural studies. *BMC biology* **13**, 66 (2015). https://doi.org:10.1186/s12915-015-0176-7

54 Willis, E. F. *et al.* Repopulating Microglia Promote Brain Repair in an IL-6-Dependent Manner. *Cell* **180**, 833-846.e816 (2020). https://doi.org:10.1016/j.cell.2020.02.013

55 Zhang, Y. *et al.* Repopulating retinal microglia restore endogenous organization and function under CX3CL1-CX3CR1 regulation. *Science advances* **4**, eaap8492 (2018). https://doi.org:10.1126/sciadv.aap8492

56 Guillaumin, M. C. C. *et al.* Deficient synaptic neurotransmission results in a persistent sleep-like cortical activity across vigilance states in mice. *bioRxiv*, 2023.2005.2011.540034 (2023). https://doi.org:10.1101/2023.05.11.540034

57 Osorio-Forero, A. *et al.* Noradrenergic circuit control of non-REM sleep substates. *Current biology : CB* **31**, 5009-5023.e5007 (2021). https://doi.org:10.1016/j.cub.2021.09.041

58 Ma, C. *et al.* Microglia Regulate Sleep via Calcium-Dependent Modulation of Norepinephrine Transmission. *bioRxiv*, 2023.2007.2024.550176 (2023). https://doi.org:10.1101/2023.07.24.550176

59 Stowell, R. D. *et al.* Noradrenergic signaling in the wakeful state inhibits microglial surveillance and synaptic plasticity in the mouse visual cortex. *Nature neuroscience* **22**, 1782-1792 (2019). https://doi.org:10.1038/s41593-019-0514-0

60 Liu, Y. U. *et al.* Neuronal network activity controls microglial process surveillance in awake mice via norepinephrine signaling. *Nature neuroscience* **22**, 1771-1781 (2019). https://doi.org:10.1038/s41593-019-0511-3

61 Maugard, M., Vigneron, P. A., Bolanos, J. P. & Bonvento, G. l-Serine links metabolism with neurotransmission. *Prog Neurobiol* **197**, 101896 (2021). https://doi.org:10.1016/j.pneurobio.2020.101896

62 Vávrová, K., Hrabálek, A., Dolezal, P., Holas, T. & Zbytovská, J. L-Serine and glycine based ceramide analogues as transdermal permeation enhancers: polar head size and hydrogen bonding. *Bioorganic & medicinal chemistry letters* **13**, 2351-2353 (2003). https://doi.org:10.1016/s0960-894x(03)00409-8

63 Masuda, T. *et al.* Novel Hexb-based tools for studying microglia in the CNS. *Nature immunology* **21**, 802-815 (2020). https://doi.org:10.1038/s41590-020-0707-4

64 Masuda, T. *et al.* Specification of CNS macrophage subsets occurs postnatally in defined niches. *Nature* **604**, 740-748 (2022). https://doi.org:10.1038/s41586-022-04596-2

65 Lei, F. *et al.* CSF1R inhibition by a small-molecule inhibitor is not microglia specific; affecting hematopoiesis and the function of macrophages. *Proceedings of the National Academy of Sciences of the United States of America* **117**, 23336-23338 (2020). https://doi.org:10.1073/pnas.1922788117

66 Mezö, C. *et al.* Different effects of constitutive and induced microbiota modulation on microglia in a mouse model of Alzheimer's disease. *Acta neuropathologica communications* **8**, 119 (2020). https://doi.org:10.1186/s40478-020-00988-5

67 Mossad, O. *et al.* Gut microbiota drives age-related oxidative stress and mitochondrial damage in microglia via the metabolite N(6)-carboxymethyllysine. *Nature neuroscience* **25**, 295-305 (2022). https://doi.org:10.1038/s41593-022-01027-3

68 Dobin, A. *et al.* STAR: ultrafast universal RNA-seq aligner. *Bioinformatics (Oxford, England)* **29**, 15-21 (2013). https://doi.org:10.1093/bioinformatics/bts635

69 Harrow, J. *et al.* GENCODE: the reference human genome annotation for The ENCODE Project. *Genome research* **22**, 1760-1774 (2012). https://doi.org:10.1101/gr.135350.111

70 Ritchie, M. E. *et al.* limma powers differential expression analyses for RNA-sequencing and microarray studies. *Nucleic acids research* **43**, e47 (2015). https://doi.org:10.1093/nar/gkv007

949 71 Ge, S. X., Jung, D. & Yao, R. ShinyGO: a graphical gene-set enrichment tool for animals and
950 plants. *Bioinformatics (Oxford, England)* **36**, 2628-2629 (2020).
951 https://doi.org:10.1093/bioinformatics/btz931
952 72 Favuzzi, E. *et al.* GABA-receptive microglia selectively sculpt developing inhibitory circuits. *Cell*
953 **184**, 5686 (2021). https://doi.org:10.1016/j.cell.2021.10.009
954 73 Behringer, S. *et al.* Targeted Metabolic Profiling of Methionine Cycle Metabolites and Redox
955 Thiol Pools in Mammalian Plasma, Cells and Urine. *Metabolites* **9** (2019).
956 https://doi.org:10.3390/metabo9100235
957 74 Bravo, A. C. *et al.* Analysis of S-Adenosylmethionine and S-Adenosylhomocysteine: Method
958 Optimisation and Profiling in Healthy Adults upon Short-Term Dietary Intervention. *Metabolites*
959 **12**, 373 (2022).
960 75 Hannibal, L. *et al.* Metabolic Profiling in Human Fibroblasts Enables Subtype Clustering in
961 Glycogen Storage Disease. *Front Endocrinol (Lausanne)* **11**, 579981 (2020).
962 https://doi.org:10.3389/fendo.2020.579981
963 76 Maier, J. P. *et al.* Inhibition of metabotropic glutamate receptor III facilitates sensitization to
964 alkylating chemotherapeutics in glioblastoma. *Cell Death Dis* **12**, 723 (2021).
965 https://doi.org:10.1038/s41419-021-03937-9
966 77 Moritz, L., Klotz, K., Grunert, S. C., Hannibal, L. & Spiekerkoetter, U. Metabolic phenotyping in
967 phenylketonuria reveals disease clustering independently of metabolic control. *Mol Genet*
968 *Metab* **138**, 107509 (2023). https://doi.org:10.1016/j.ymgme.2023.107509
969 78 Franken, P., Malafosse, A. & Tafti, M. Genetic variation in EEG activity during sleep in inbred
970 mice. *The American journal of physiology* **275**, R1127-1137 (1998).
971 https://doi.org:10.1152/ajpregu.1998.275.4.R1127
972 79 Li, S., Franken, P. & Vassalli, A. Bidirectional and context-dependent changes in theta and
973 gamma oscillatory brain activity in noradrenergic cell-specific Hypocretin/Orexin receptor 1-KO
974 mice. *Scientific reports* **8**, 15474 (2018). https://doi.org:10.1038/s41598-018-33069-8
975 80 Tort, A. B. *et al.* Dynamic cross-frequency couplings of local field potential oscillations in rat
976 striatum and hippocampus during performance of a T-maze task. *Proc Natl Acad Sci U S A* **105**,
977 20517-20522 (2008). https://doi.org:10.1073/pnas.0810524105

978

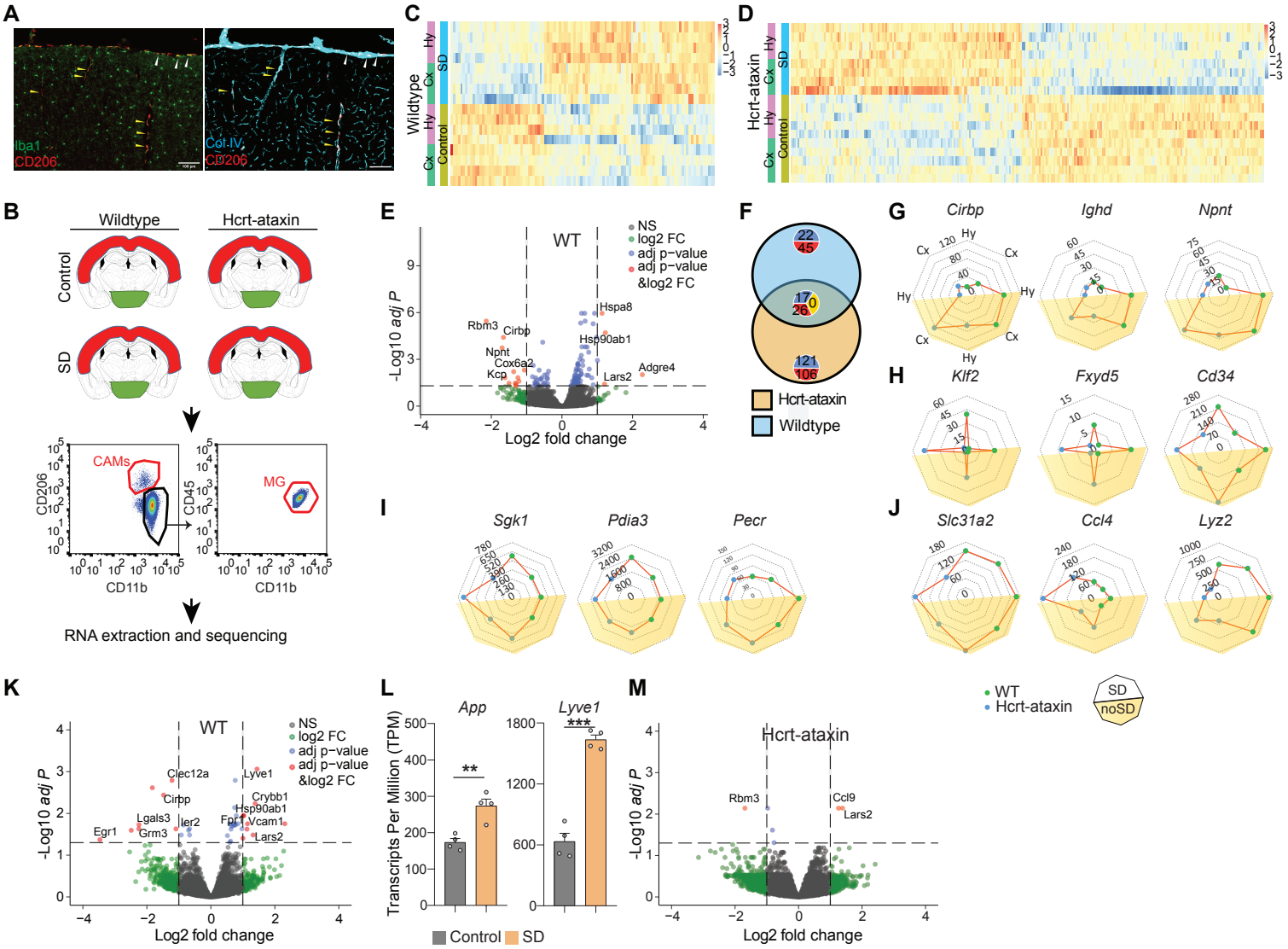
A
Iba1
CD206
Col IV
CD206
B
Wildtype
Hcrt-ataxin
Control
SD
CAMs
MG
CD206
CD45
CD11b
CD11b
RNA extraction and sequencing
C
Wildtype
Hy
Cx
SD
Control
D
Hcrt-ataxin
E
WT
NS
log2 FC
adj p−value
adj p−value &log2 FC
-Log10 adj P
Log2 fold change
Rbm3
Cirbp
Hspa8
Hsp90ab1
Npnt
Cox6a2
Kcp
Lars2
Adgre4
F
22
45
17
26
0
121
106
Hcrt-ataxin
Wildtype
G
Cirbp
Ighd
Npnt
H
Klf2
Fxyd5
Cd34
I
Sgk1
Pdia3
Pecr
J
Slc31a2
Ccl4
Lyz2
K
WT
NS
log2 FC
adj p−value
adj p−value &log2 FC
-Log10 adj P
Log2 fold change
Clec12a
Lyve1
Cirbp
Crybb1
Hsp90ab1
Lgals3
Egr1
Grm3
Ier2
Fpr1
Vcam1
Lars2
L
App
Lyve1
Transcripts Per Million (TPM)
**
***
Control
SD
M
Hcrt-ataxin
-Log10 adj P
Log2 fold change
Rbm3
Ccl9
Lars2
WT
Hcrt-ataxin
SD
noSD

Fig. 1.

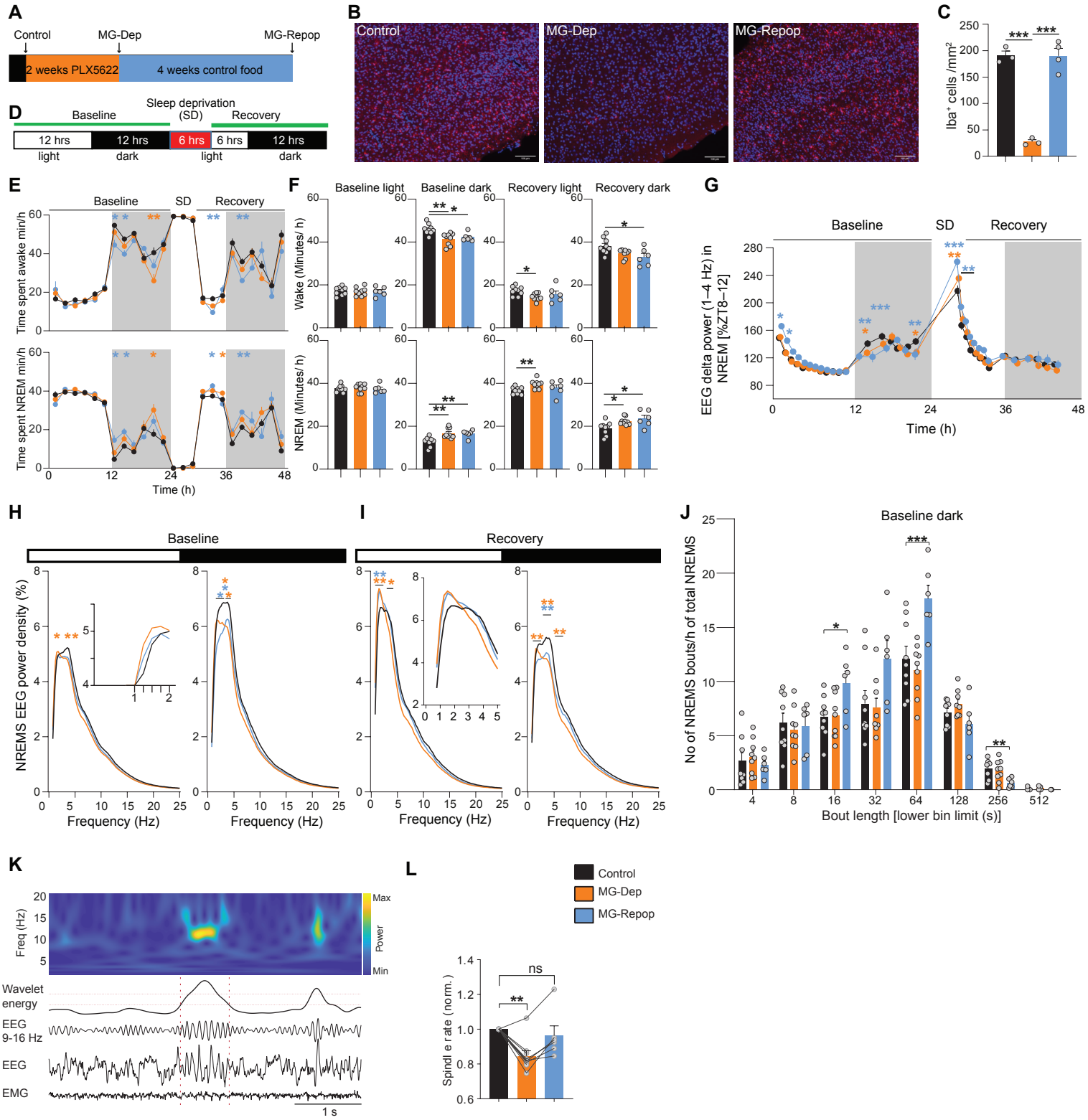
A
Control
MG-Dep
MG-Repop
2 weeks PLX5622
4 weeks control food
B
Control
MG-Dep
MG-Repop
C
Iba+ cells /mm2
D
Baseline
Sleep deprivation (SD)
Recovery
12 hrs light
12 hrs dark
6 hrs light
6 hrs
12 hrs dark
E
Baseline
SD
Recovery
Time spent awake min/h
Time spent NREM min/h
Time (h)
F
Baseline light
Baseline dark
Recovery light
Recovery dark
Wake (Minutes/ h)
NREM (Minutes/ h)
G
Baseline
SD
Recovery
EEG delta power (1–4 Hz) in NREM [%ZT8–12]
Time (h)
H
Baseline
NREMS EEG power density (%)
Frequency (Hz)
I
Recovery
Frequency (Hz)
J
Baseline dark
No of NREMS bouts/h of total NREMS
Bout length [lower bin limit (s)]
K
Freq (Hz)
Max
Power
Min
Wavelet energy
EEG 9-16 Hz
EEG
EMG
1 s
L
Control
MG-Dep
MG-Repop
ns
Spindle rate (norm.)

Fig. 2

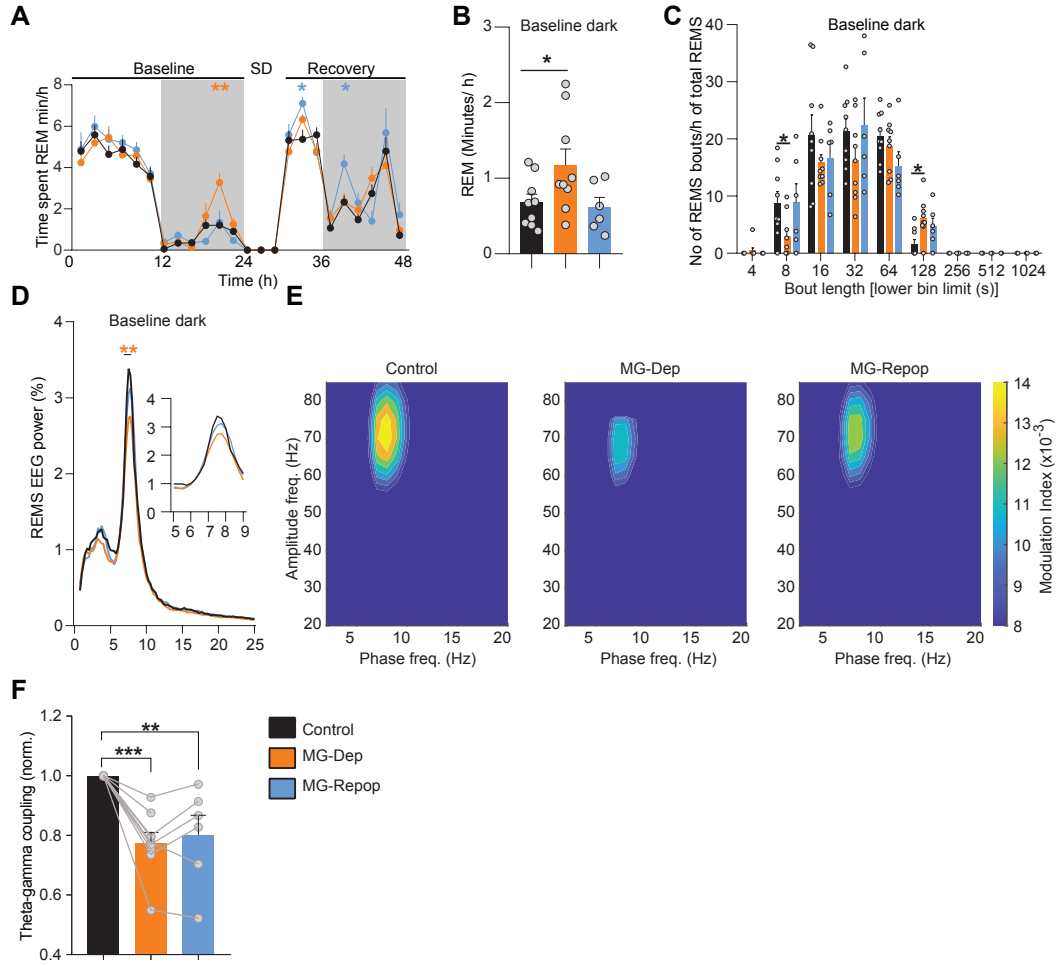
A
Baseline
SD
Recovery
Time spent REM min/h
Time (h)
B
Baseline dark
REM (Minutes/ h)
C
Baseline dark
No of REMS bouts/h of total REMS
Bout length [lower bin limit (s)]
D
Baseline dark
REMS EEG power (%)
E
Control
MG-Dep
MG-Repop
Amplitude freq. (Hz)
Phase freq. (Hz)
Modulation Index (x10-3)

F
Theta-gamma coupling (norm.)
Control
MG-Dep
MG-Repop

Fig. 3.

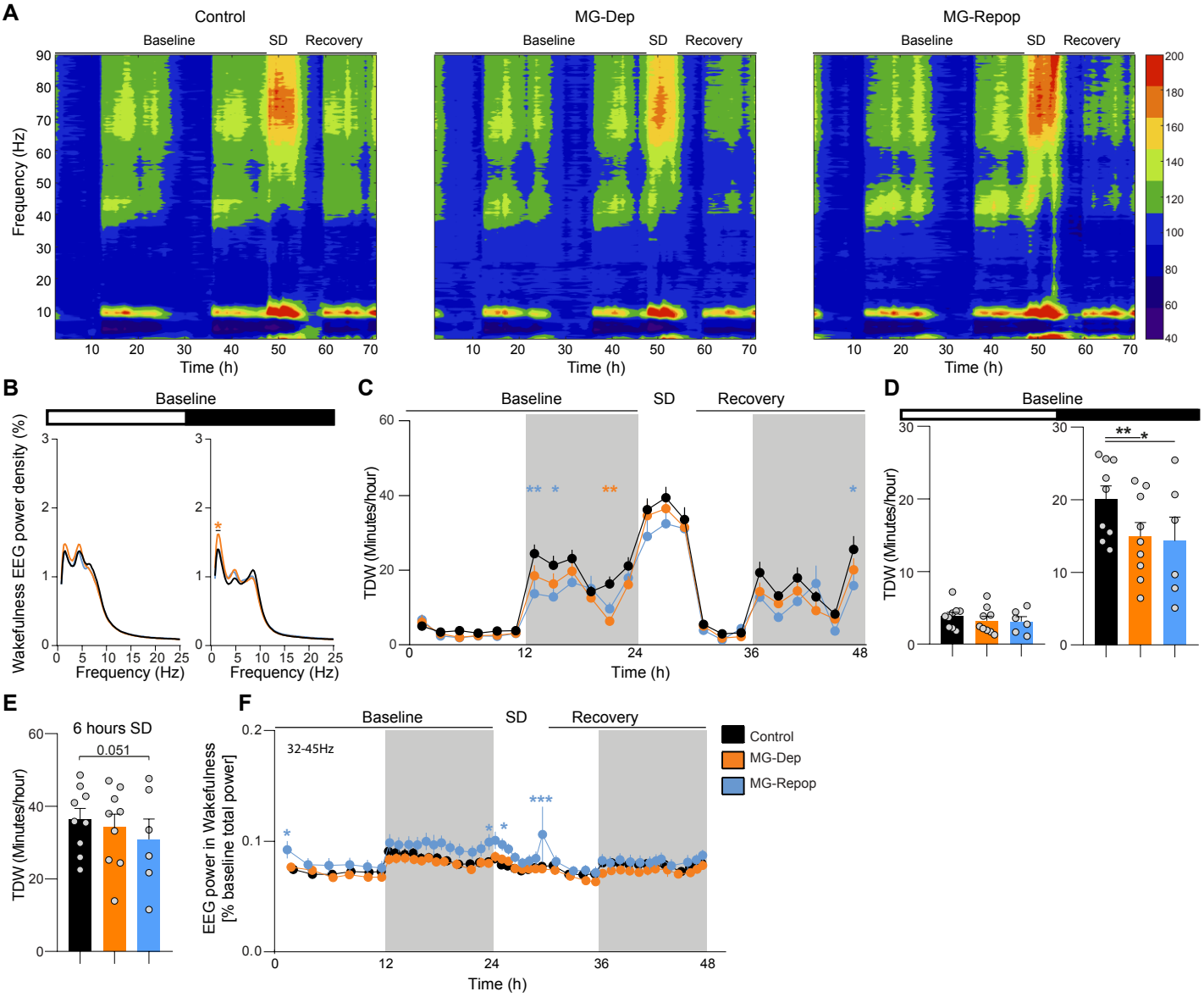
A
Control
MG-Dep
MG-Repop
Baseline
SD
Recovery
Frequency (Hz)
Time (h)
B
Baseline
Wakefulness EEG power density (%)
Frequency (Hz)
C
Baseline
SD
Recovery
TDW (Minutes/hour)
Time (h)
D
Baseline
TDW (Minutes/hour)
E
6 hours SD
0.051
TDW (Minutes/hour)
F
Baseline
SD
Recovery
32-45Hz
EEG power in Wakefulness [% baseline total power]
Time (h)
Control
MG-Dep
MG-Repop

Fig. 4

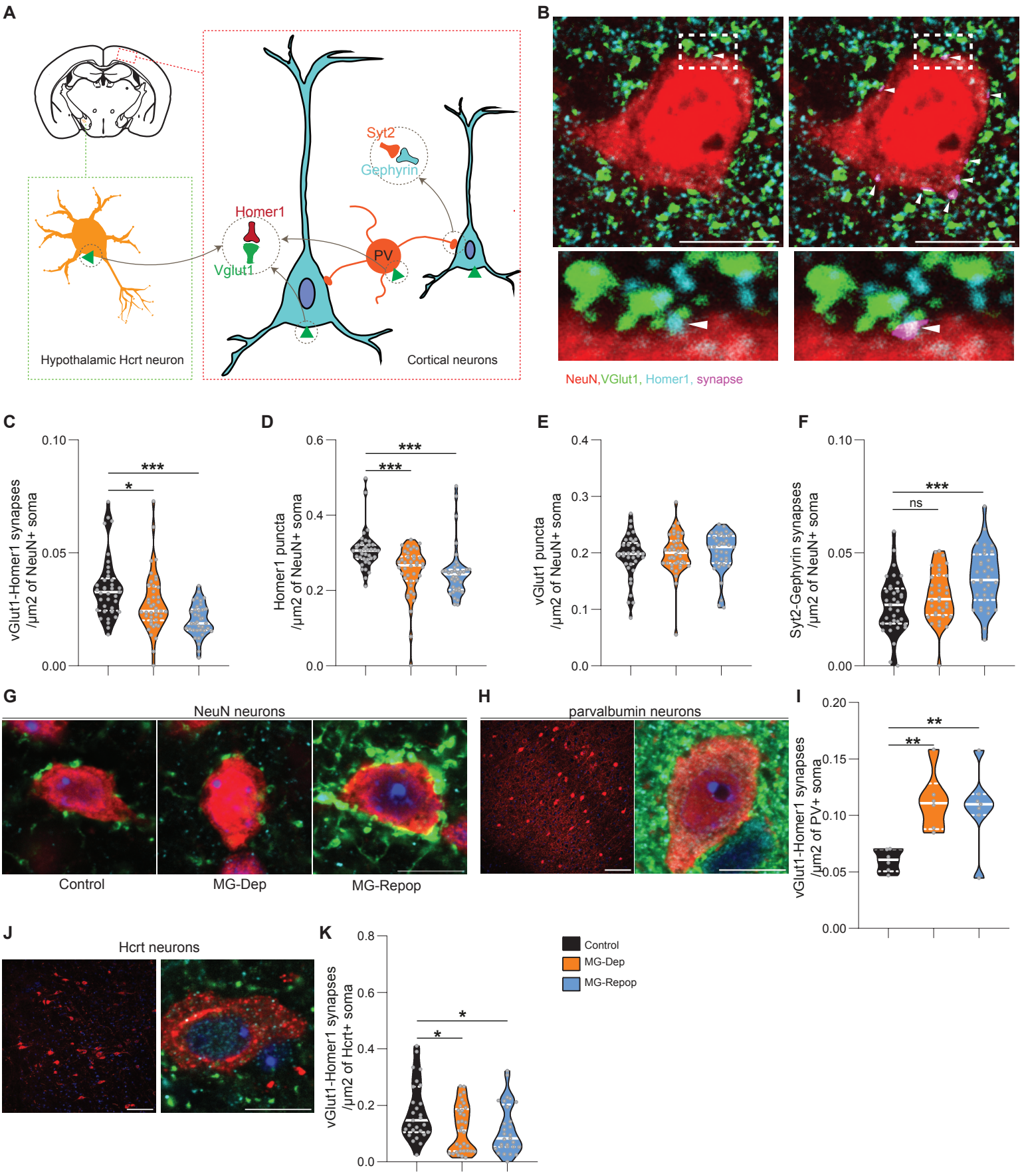
A
Syt2
Gephyrin
Homer1
Vglut1
PV
Hypothalamic Hcrt neuron
Cortical neurons
B
NeuN,VGlut1, Homer1, synapse
C
vGlut1-Homer1 synapses /µm2 of NeuN+ soma
D
Homer1 puncta /µm2 of NeuN+ soma
E
vGlut1 puncta /µm2 of NeuN+ soma
F
Syt2-Gephyrin synapses /µm2 of NeuN+ soma
ns
G
NeuN neurons
Control
MG-Dep
MG-Repop
H
parvalbumin neurons
I
vGlut1-Homer1 synapses /µm2 of PV+ soma
J
Hcrt neurons
K
vGlut1-Homer1 synapses /µm2 of Hcrt+ soma
Control
MG-Dep
MG-Repop

Fig. 5

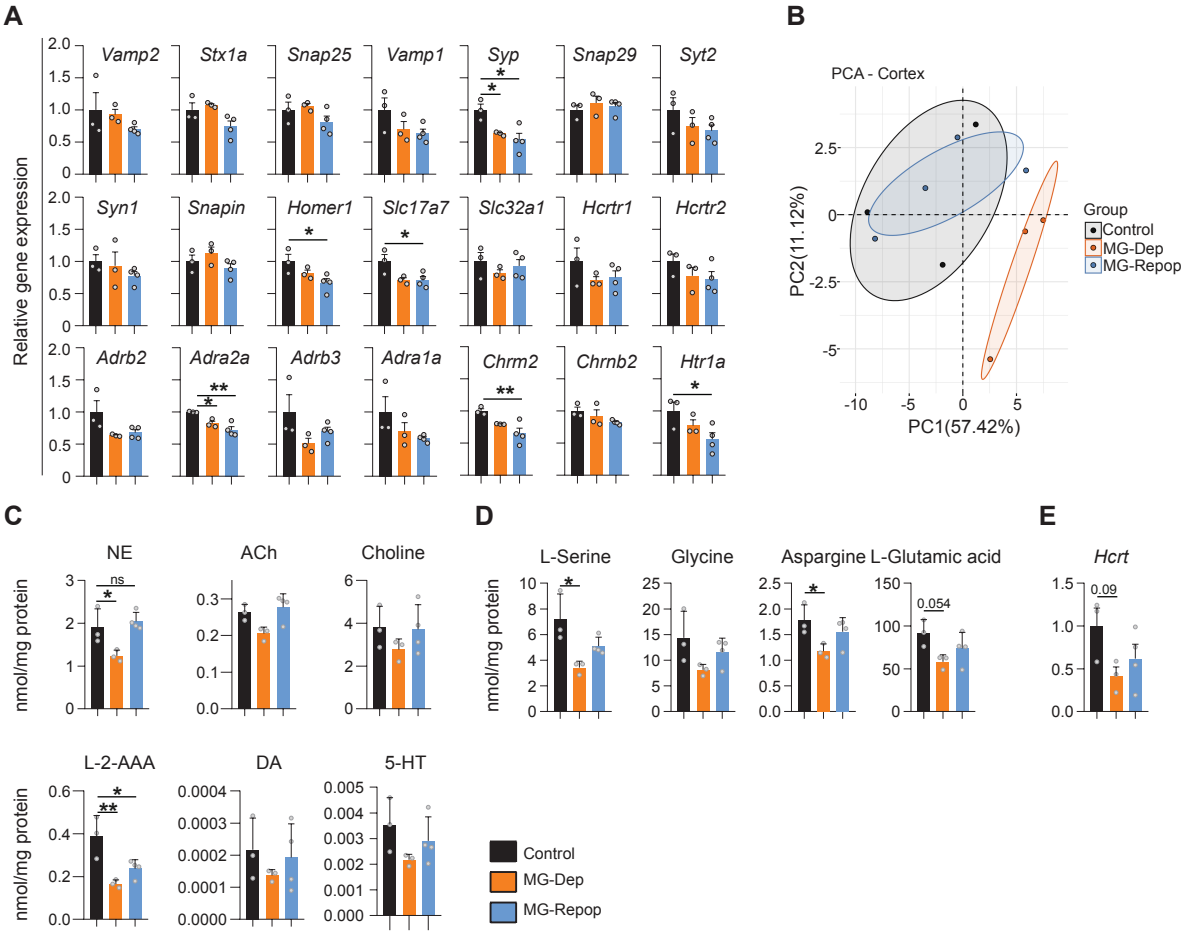
A
Relative gene expression
Vamp2
Stx1a
Snap25
Vamp1
Syp
Snap29
Syt2
Syn1
Snapin
Homer1
Slc17a7
Slc32a1
Hcrtr1
Hcrtr2
Adrb2
Adra2a
Adrb3
Adra1a
Chrm2
Chrnb2
Htr1a
B
PCA - Cortex
PC2(11.12%)
PC1(57.42%)
Group
Control
MG-Dep
MG-Repop
C
NE
ACh
Choline
L-2-AAA
DA
5-HT
nmol/mg protein
ns
D
L-Serine
Glycine
Aspargine
L-Glutamic acid
0.054
E
Hcrt
0.09
Control
MG-Dep
MG-Repop

Fig. 6.

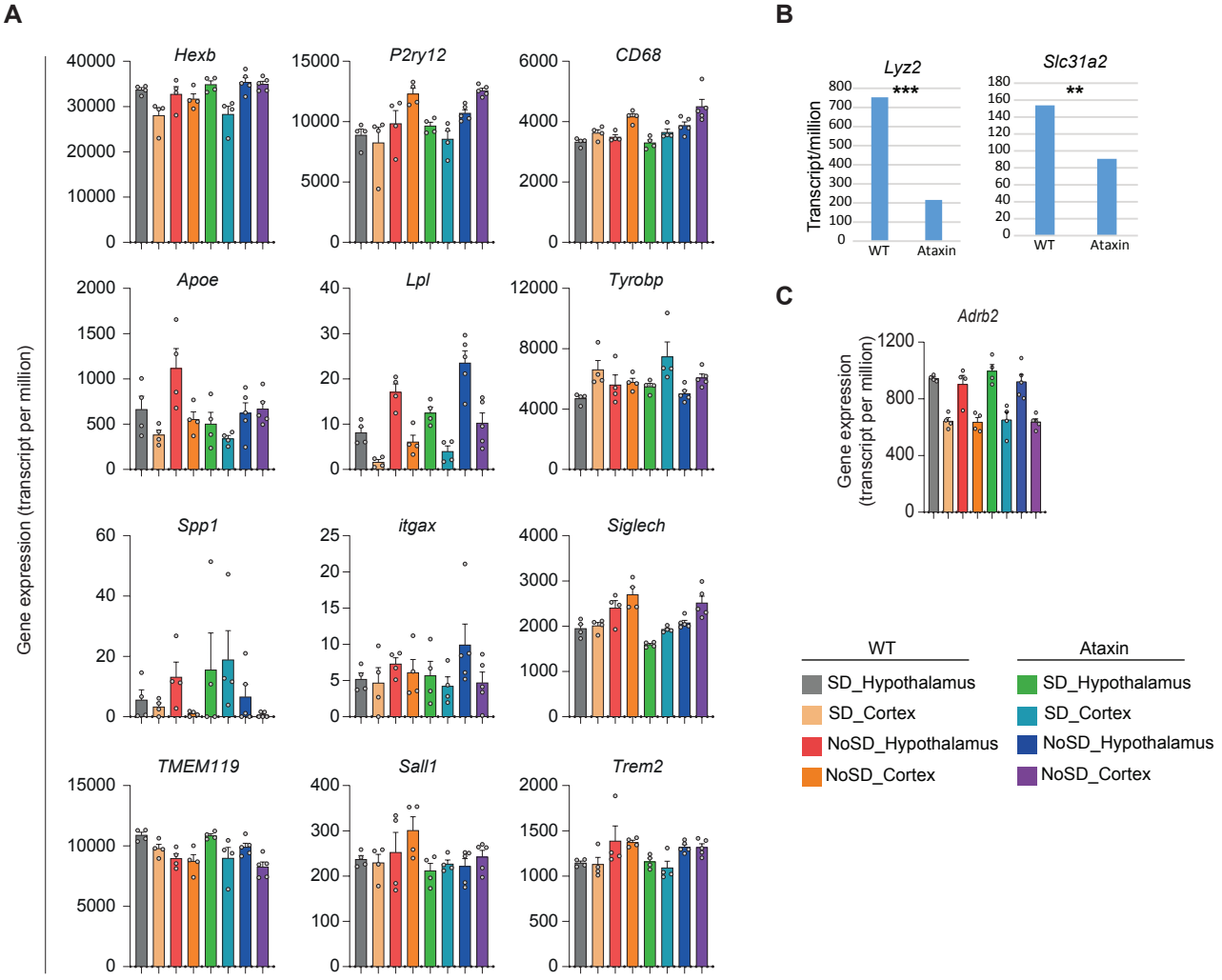
A
Gene expression (transcript per million)
Hexb
P2ry12
CD68
Apoe
Lpl
Tyrobp
Spp1
itgax
Siglech
TMEM119
Sall1
Trem2
B
Lyz2
Slc31a2
Transcript/million
***
**
WT
Ataxin
C
Adrb2
Gene expression (transcript per million)
WT
SD_Hypothalamus
SD_Cortex
NoSD_Hypothalamus
NoSD_Cortex
Ataxin
SD_Hypothalamus
SD_Cortex
NoSD_Hypothalamus
NoSD_Cortex

Fig. S1

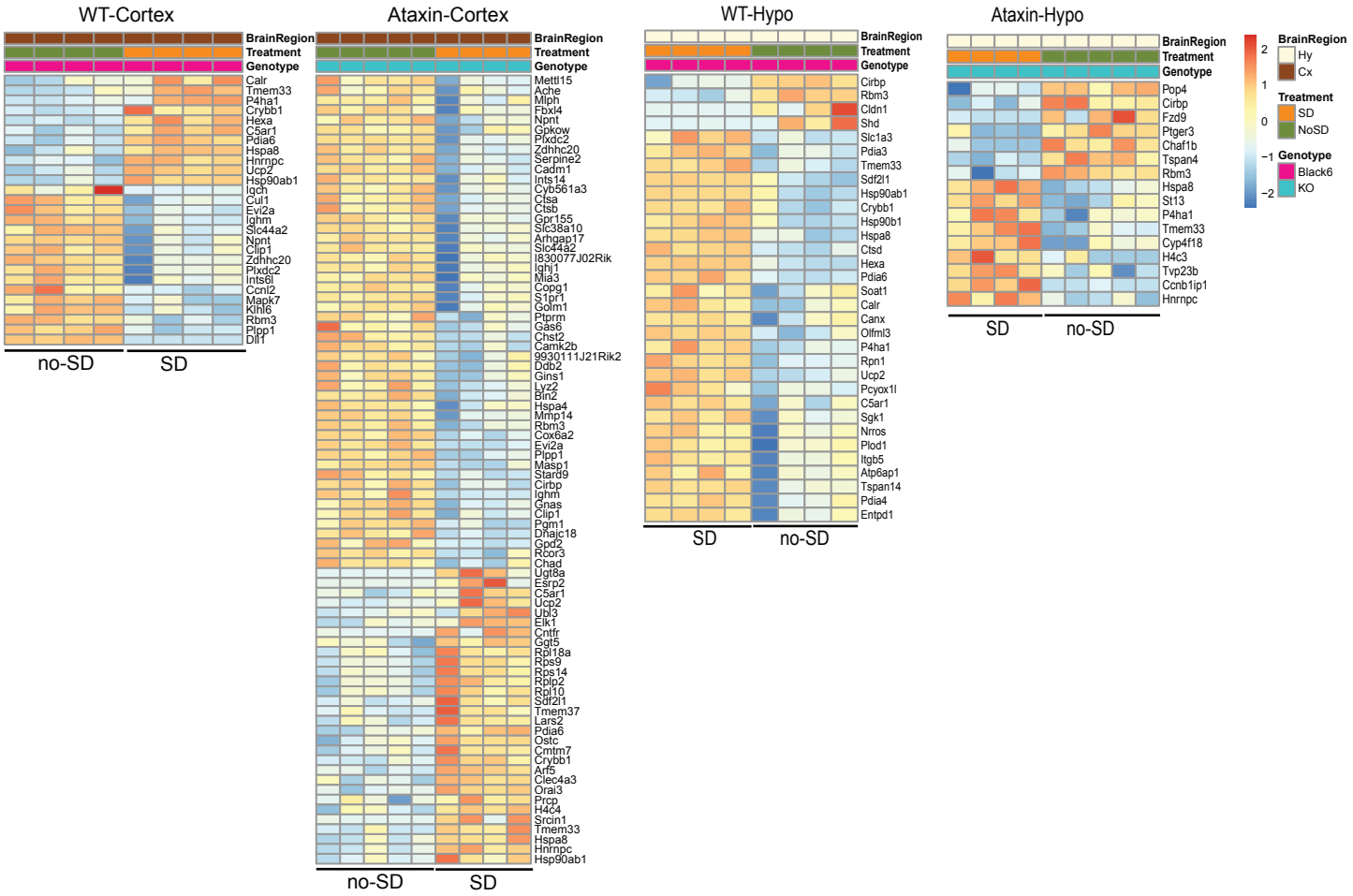
WT-Cortex
Ataxin-Cortex
WT-Hypo
Ataxin-Hypo
BrainRegion
Treatment
Genotype
Calr
Tmem33
P4ha1
Crybb1
Hexa
C5ar1
Pdia6
Hspa8
Hnrnpc
Ucp2
Hsp90ab1
Igch
Cul1
Evi2a
Ighm
Slc44a2
Npnt
Clip1
Zdhhc20
Plxdc2
Ints6l
Ccnl2
Mapk7
Klhl6
Rbm3
Plpp1
Dll1
no-SD
SD
Mettl15
Ache
Mlph
Fbxl4
Npnt
Gpkow
Plxdc2
Zdhhc20
Serpine2
Cadm1
Ints14
Cyb561a3
Ctsa
Ctsb
Gpr155
Slc38a10
Arhgap17
Slc44a2
I830077J02Rik
Ighj1
Mia3
Copg1
S1pr1
Golm1
Ptprm
Gas6
Chst2
Camk2b
9930111J21Rik2
Ddb2
Gins1
Lyz2
Bin2
Hspa4
Mmp14
Rbm3
Cox6a2
Evi2a
Plpp1
Masp1
Stard9
Cirbp
Ighm
Gnas
Clip1
Pgm1
Dnajc18
Gpd2
Rcor3
Chad
Ugt8a
Esrp2
C5ar1
Ucp2
Ubl3
Elk1
Cntfr
Ggt5
Rpl18a
Rps9
Rps14
Rplp2
Rpl10
Sdf2l1
Tmem37
Lars2
Pdia6
Ostc
Cmtm7
Crybb1
Arf5
Clec4a3
Orai3
Prcp
H4c4
Srcin1
Tmem33
Hspa8
Hnrnpc
Hsp90ab1
Cirbp
Rbm3
Cldn1
Shd
Slc1a3
Pdia3
Tmem33
Sdf2l1
Hsp90ab1
Crybb1
Hsp90b1
Hspa8
Ctsd
Hexa
Pdia6
Soat1
Calr
Canx
Olfml3
P4ha1
Rpn1
Ucp2
Pcyox1l
C5ar1
Sgk1
Nrros
Plod1
Itgb5
Atp6ap1
Tspan14
Pdia4
Entpd1
Pop4
Cirbp
Fzd9
Ptger3
Chaf1b
Tspan4
Rbm3
Hspa8
St13
P4ha1
Tmem33
Cyp4f18
H4c3
Tvp23b
Ccnb1ip1
Hnrnpc
2
1
0
−1
−2
BrainRegion
Hy
Cx
Treatment
SD
NoSD
Genotype
Black6
KO

Fig. S2

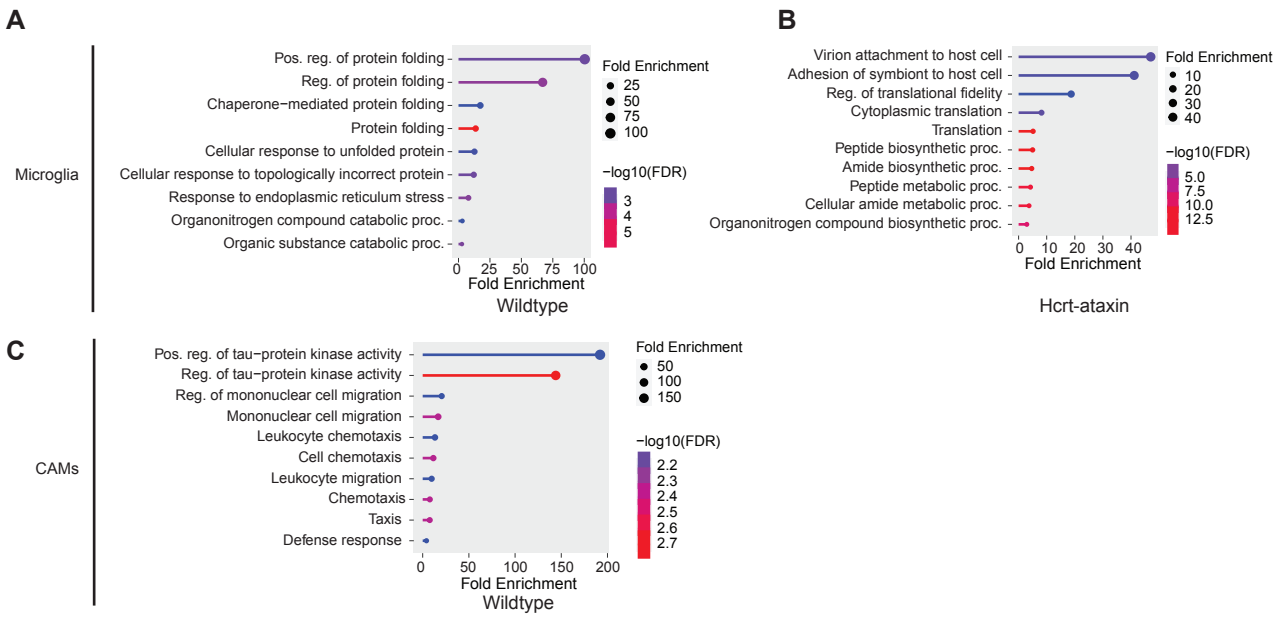
A
Microglia
Pos. reg. of protein folding
Reg. of protein folding
Chaperone−mediated protein folding
Protein folding
Cellular response to unfolded protein
Cellular response to topologically incorrect protein
Response to endoplasmic reticulum stress
Organonitrogen compound catabolic proc.
Organic substance catabolic proc.
0 25 50 75 100
Fold Enrichment
Wildtype
Fold Enrichment
25
50
75
100
−log10(FDR)
3
4
5
B
Virion attachment to host cell
Adhesion of symbiont to host cell
Reg. of translational fidelity
Cytoplasmic translation
Translation
Peptide biosynthetic proc.
Amide biosynthetic proc.
Peptide metabolic proc.
Cellular amide metabolic proc.
Organonitrogen compound biosynthetic proc.
0 10 20 30 40
Fold Enrichment
Hcrt-ataxin
Fold Enrichment
10
20
30
40
−log10(FDR)
5.0
7.5
10.0
12.5
C
CAMs
Pos. reg. of tau−protein kinase activity
Reg. of tau−protein kinase activity
Reg. of mononuclear cell migration
Mononuclear cell migration
Leukocyte chemotaxis
Cell chemotaxis
Leukocyte migration
Chemotaxis
Taxis
Defense response
0 50 100 150 200
Fold Enrichment
Wildtype
Fold Enrichment
50
100
150
−log10(FDR)
2.2
2.3
2.4
2.5
2.6
2.7

Fig. S3